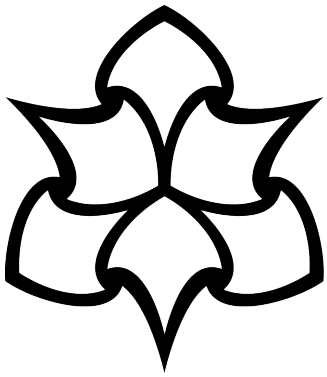

Ordered Diamond Nanowire Growth on Mesoporous Silica Oxides Using Hot Filament Chemical Vapour Deposition -

A Feasibility Study

Iain Wilson

A thesis submitted in partial fulfilment of the requirements of the
Manchester Metropolitan University
for the degree of MSc (by research)

Faculty of Science and Engineering the
Manchester Metropolitan University 2012

Abstract

The concept of growing ordered diamond nanowires using HFCVD is investigated in this research. Modified mesoporous silicas are synthesized as possible substrates for diamond nanowire growth and their structures are examined using nitrogen porosimmetry. HFCVD is used initially to grow diamond coatings on silicon wafer before the novel use of the technique to attempt the first growth of ordered diamond nanowires using mesoporous silica as a template. The findings of this research show the conditions for growth of diamond using the CVD technique may be, however, outside of the conditions within which the mesoporous silicas are very stable. At a temperature that shows good deposition on flat substrates the results suggest, with a decrease in overall mass of the sample, that there may be a breakdown of the porous structure of the silicas.

Contents

Acknowledgements

I would like to thank my wife Siobhán Wilson for being so patient throughout my research and write up, her support has been invaluable and without it this document would never have been completed.

My supervisors Dr Aidan Doyle and Dr Chris Rego provided excellent backing in order to keep this project on-going. Their expertise in the areas of mesoporous materials and Diamond Chemical Vapour Deposition were called upon frequently, with help and advice given freely.

Thanks also go to my mother and my father their financial support throughout was essential, as ever, I am indebted.

1

INTRODUCTION

1.1: Zeolites.

Most mesoporous oxides are similar to zeolites, the name zeolite from two Greek words “zein” and “lithos”, meaning “boiling stone”.[1,2] A zeolite can be described as a type of sponge, they are crystalline solids with perfect micro-porous structures.[3] Zeolites consist of lattice framework of $[SiO_4]^{4-}$/$[AlO_4]^{5-}$ tetrahedras forming cage type structures, commonly known as Sodalite cages.[4] Secondary building blocks made up of the same tetrahedra as the basic Sodalite cages form with these to make the zeolite solid structure.[6]

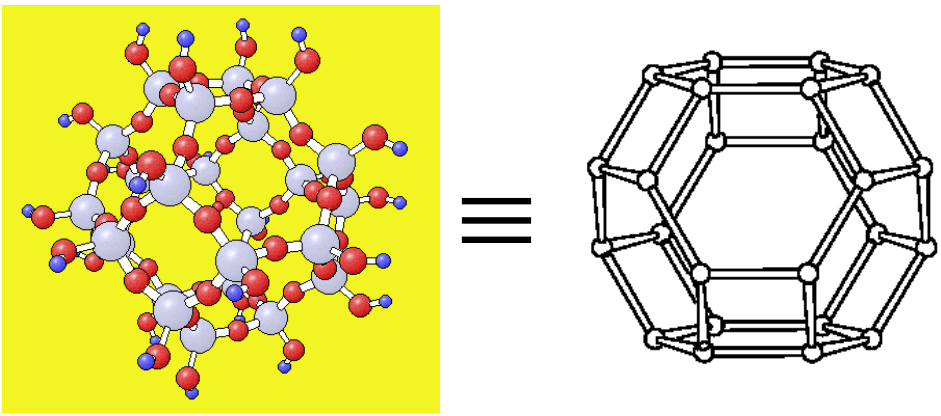

Fig 1.0: the basic structure of a sodalite cage, left, atomic model, right, cage structure.[4,5]

In accordance with IUPAC definitions, porous materials are divided into three classes according to pore diameter, microporous (<2 nm), mesoporous (2-50 nm) and macroporous (>50 nm).[7] This makes a zeolite a typical microporous material, and, even despite the success of zeolites, their applications are limited by the relatively small pore openings, therefore, pore enlargement, effectively the development of mesoporous and macroporous materials was a strong focus for zeolite chemistry.[8]

1.2: Mesoporous Materials

1.2.1: Historical Aspects

The first mesoporous materials to be synthesised were called MCM (Mobil Composition of Matter), in particular MCM-41 materials synthesised in 1991 were of interest, as they were the first high surface area (>1000 $m^2 g^{-1}$) mesoporous solids that showed regularly ordered pore arrangements and very narrow pore size distributions.[9,10] A procedure for the synthesis of MCM-41 had been patented in 1969, however it was only known as a low-density silica.[11] It took until 1991 when Di Renzo et al. reproduced the synthesis reported in the patent and found that it leads to the synthesis of a material identical to mesoporous MCM-41, which scientists of the Mobil Oil Corporation patented in 1991.[12,13] The first of the materials of high surface area mesoporous materials with a large pore size, 50 to 300 Angstrom, were developed by Dongyuan Zhao Et. Al. in California in late 1997.[14] The material produced was named SBA-15, two theoretical uses at the time of first production were as a molecular sieve and separation reactions of larger molecules.[15] More recent uses include photocatalysis applications and the growth by Chemical Vapour Deposition (CVD), or nanocasting, of other materials.[16-19]

1.2.2: Mechanism of Formation

1.2.2.1: Synthesis

The original MCM synthesis, from 1991, was conducted in water under alkaline conditions.[9,10] Silica was added to a basic surfactant solution and the contents were heated at 100/150ºC in a sealed container for 24/48 hours. In a similar manner to zeolite synthesis, organic surfactant molecules function as templates forming an ordered organic-inorganic composite material.[20] The surfactant is then removed by

calcination in air, or by solvent extraction, leaving a porous silicate network.[21] In contrast to zeolites however, the templates used for MCM synthesis are not single organic molecules but liquid-crystalline self-assembled surfactant molecules.

The formation of the inorganic-organic composites is based on electrostatic interactions between the surfactant and silicate species and several studies have shown that the formation of MCM-41 follows a 'liquid crystal templating' (LCT) mechanism (figure 1.1).[10,22]

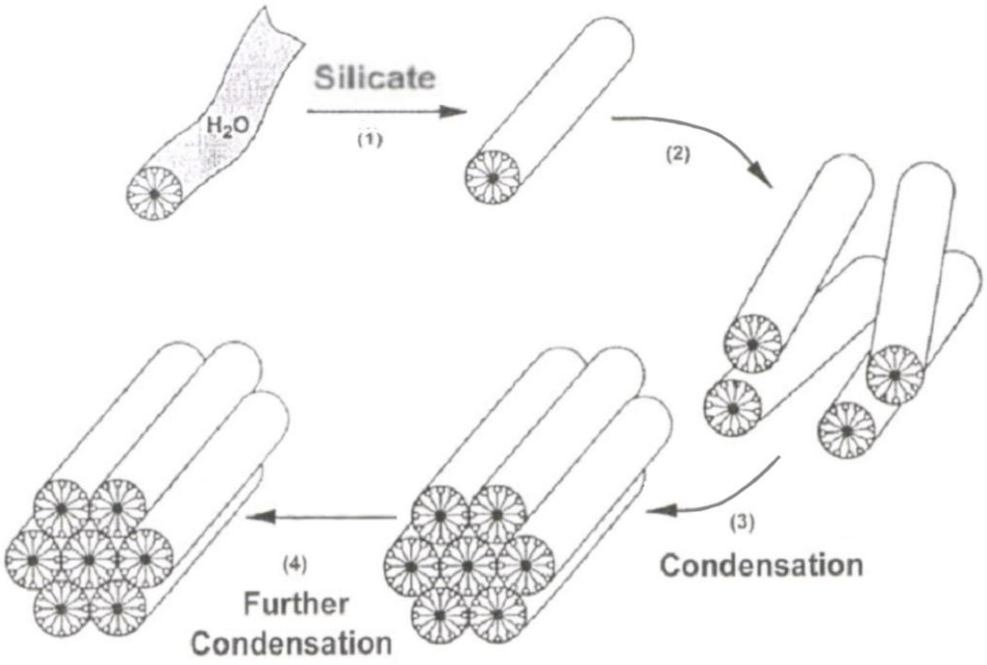

Fig. 1.1: MCM-41 formation showing liquid crystal templating method of cooperative self-assembly: (1) TEOS hyrolisation around a surfactant. (2) The Silicate assembles into rows. (3&4) The Silicate condenses around the surfactant to form MCM-41.[10]

In this mechanism, the silica, tetraethyl orthosilicate (TEOS), shown in figure 1.2, firstly, hydrolyses in the water, and secondly condenses around the surfactant molecules.

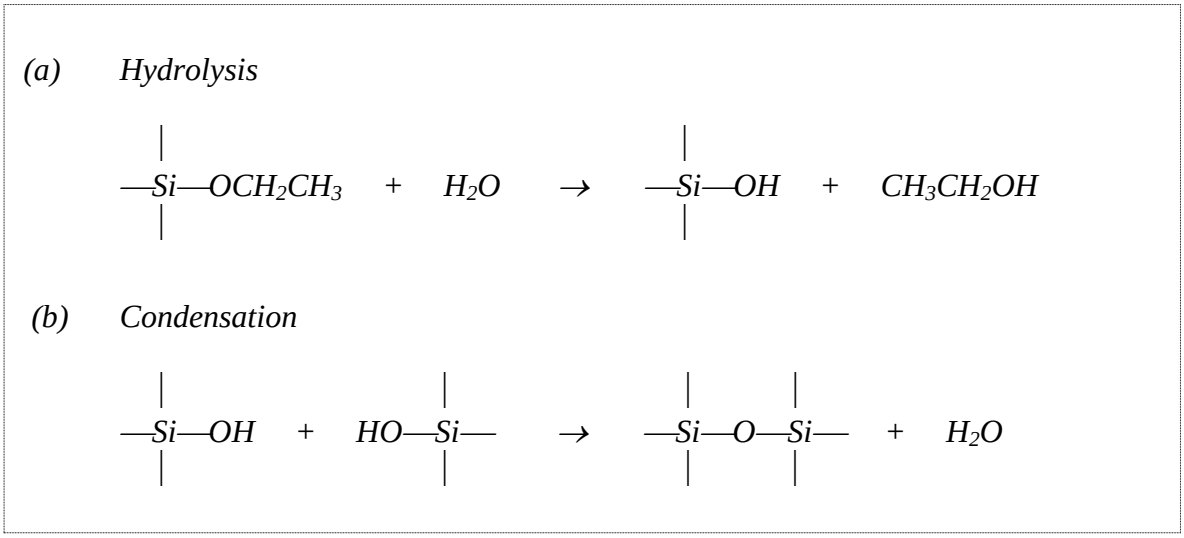

Fig 1.2: reactions of silica source TEOS in LCT mechanism for synthesis of MCM

Whilst MCM-41 is made under alkali conditions, SBA-15 formation, shown here in fig 1.3, is under acidic conditions.[14,23] In forming SBA-15, the sample can be heated over a range of times and temperatures, with a window of silica concentration also effective in the formation of SBA-15.[14,23,24] Different heating times, temperatures and silica concentrations cause differences in silica wall thicknesses and pore size.[14]

As with MCM-41,there is an electrostatic driving force behind the reaction. Silica is hydrolysed forming $Si(OMe)_{4-n}(OH_2^+)_n$ electrostatic reactions of Cl^- and Van der Waals forces then form the silica microstructures.[25,26]

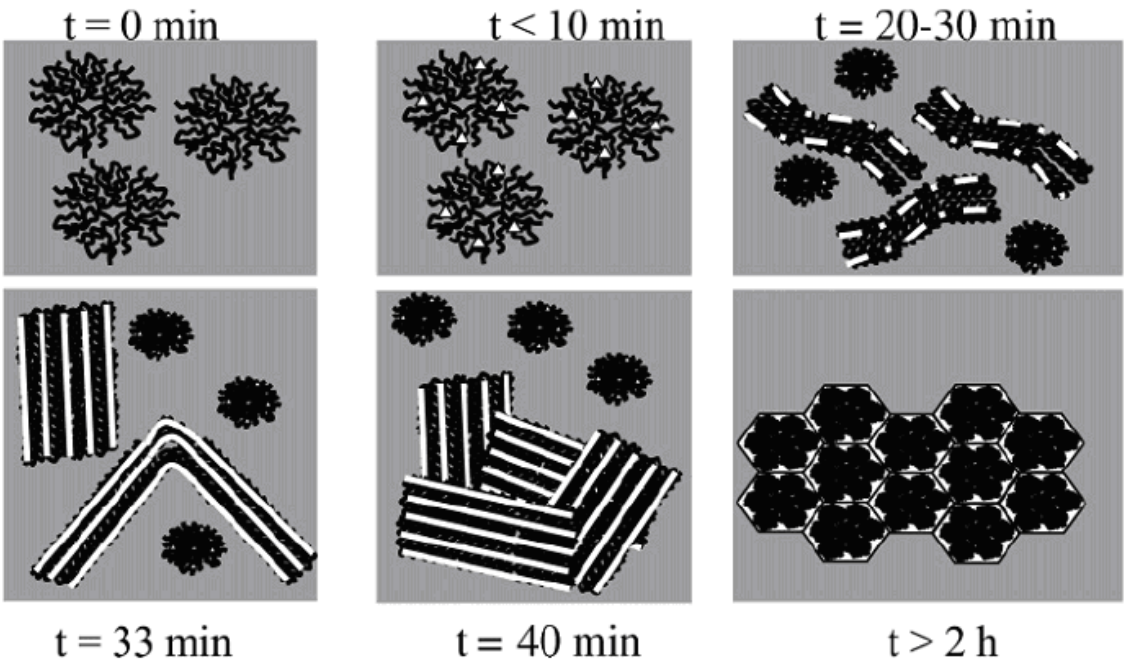

Fig 1.3: A schematic model summarising the production of microstructures in the formation of SBA-15. This model shows that the hexagonal structure is formed only in the later times of the sample preparation (t > 2 h).[27]

1.2.2.2: Bond Formations

The drive behind the condensation of the silicate onto the surfactant surface is one of ionic attraction. The organization of cationic quaternary ammonium surfactants (S^+) e.g. CTAB (cetyltrimethylammoniumbromide) and anionic silicate species (I^-) produces three-dimensional periodic biphase arrays. The silicate ions are attracted to the surfactant and condense, or polymerase, to form silicate walls. Cooperative interactions between inorganic and organic species based on charge interaction can also be achieved by using reverse charge matching (S^-I^+) or by mediated combinations of cationic or anionic surfactants and corresponding inorganic species ($S^+X^-I^+$, X^- = halide, or $S^-M^+I^-$, M^+ = alkali metal ion).[28,29]

The liquid-crystal approach also includes two additional pathways showing organic-inorganic interaction. Under neutral conditions, mesostructures are formed by using neutral, (S^0) or non-ionic surfactants (N^0) e.g. n-dodecylamine.[30,31] In this approach ((S^0/N^0)I^0) hydrogen bonding is considered to be the driving force for the formation of the mesophase.

1.2.2.3: Surfactant Mesophase Structural Importance

Since the liquid-crystal structures of the surfactant serve as an organic template, the behaviour of the surfactant in binary surfactant/water systems is crucial in controlling the properties of silica mesostructures.[32,33] MCM-41 can be synthesised with surfactant concentrations as low as the critical micelle concentration (CMC) and up to concentrations where liquid crystals are formed.[34] According to a microscopic model introduced by Israelachvili *et al*. the relative stabilities of different aggregate shapes and the corresponding mesophase structures can be predicted.[35] The preferred shape of self-assembled surfactant molecules above the CMC depends on the effective mean molecular parameters that establish the value of a dimensionless packing parameter *g*, which is defined in equation 1.0

$$g = \frac{V}{a_o l_c} \qquad \textbf{Eqn. 1.0}$$

where: V = effective volume of the hydrophobic chain

a_o = mean aggregate surface area per hydrophilic head group

l_c = critical hydrophobic chain length

The parameter *g* depends on the molecular geometry of the surfactant molecules, such as the number of carbon atoms in the hydrophobic chain, the degree of chain saturation, along with the size and charge of the polar head group. In addition, the effects of solution conditions, including ionic strength, pH, co-surfactant concentration and temperature, are included implicitly in V, a_o and l_c.[36] In classical micelle chemistry, mesophase transitions occur when the *g* value exceeds critical values shown here in Table 1.1 along with their mesophase structures in figure 1.4.

Dimensionless packing parameter/g	**Expected mesophase structure**	**Mesoporous Material**
1/3	*Cubic (Pm3n)*	*SBA-1*
½	*Hexagonal (p6)*	*MCM-41*
1/2-2/3	*Cubic (Ia3d)*	*MCM-48*
1/1	*Lamellar*	*MCM-50*

Table 1.1: Surfactant packing parameter *g*, expected mesopore structure and examples for each structure.

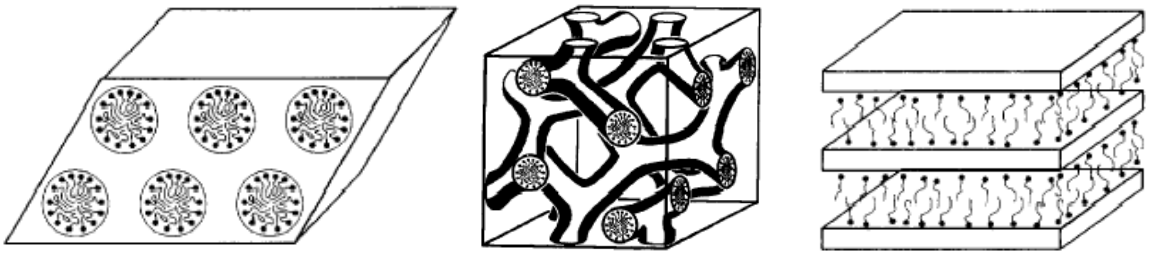

(a) **(b)** **(c)**

Fig. 1.4: Structures of (a) hexagonal phase MCM-41, (b) bicontinuous cubic phase MCM-48 and (c) lamellar MCM-50. [37]

The phase transitions also reflect a decrease in surface curvature in the micelle, from the cubic (*Pm3n*) over the hexagonal, to the lamellar phase. Spherical aggregates are preferentially formed by surfactants possessing large polar head groups. Rod-like lamellar aggregates are formed when the head groups are small and packed tightly thereby increasing the aggregation number. By including the inorganic component, Stucky *et al*. expanded the model to the NaOH/CTAB/TEOS system and created a phase diagram of mesophase structure.[38,39]

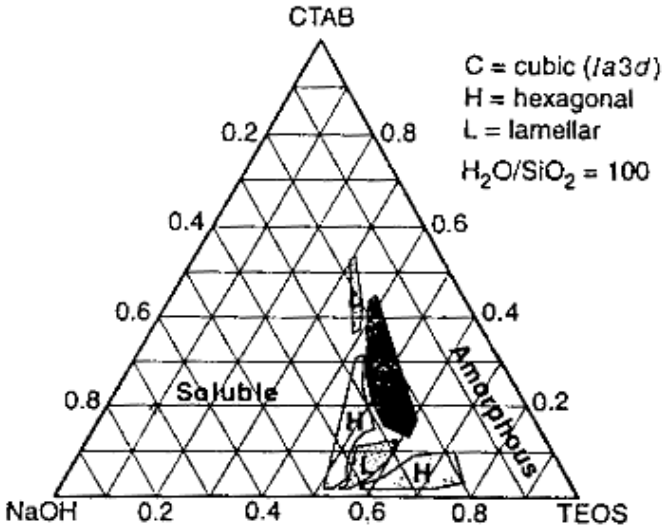

Fig. 1.5: Synthesis-space diagram of mesophase structures established by XRD measurements for synthesis using NaOH/ CTAB/TEOS synthesis. (shaded area refers to cubic structure C).[39]

Figure 1.5 shows the parameters required for synthesis of cubic, hexagonal and lamellar mesophases and outlines the conditions where amorphous, rather than ordered porous materials are formed. By using X-Ray Diffraction (XRD), Nuclear Magnetic Resonance (NMR), and polarized microscopy, both binary and ternary systems were investigated in great detail by Firouzi *et al*.[32] Vartuli *et al*. studied the effect of surfactant/silica ratios on the formation of mesostructures.[40] This ratio is a

critical variable in the mesophase formation and by varying this ratio from 0.5 to 2.0 products with hexagonal, cubic and lamellar structures were obtained.

1.2.3: Characterisation

1.2.3.1: X-ray Diffraction

The periodic arrangement of atoms in a crystal causes the diffraction of X-rays from certain planes throughout the structure. For a fixed X-ray wavelength, the angle of diffraction varies for different planes. For a maximum to occur in the diffraction pattern at a particular angle of incidence θ (with respect to planes *(hkl)*), the Bragg equation must be satisfied:

$$n\lambda = 2d_{hkl}sin\theta_{hkl} \qquad \textbf{Eqn. 1.1}^{[41]}$$

where: d_{hkl} = interplanar distance between (*hkl*) planes

n = order of reflection

λ = wavelength of incident x-rays

θ_{hkl} = diffraction angle

MCM-41 has an ordered structure that is the result of a hexagonal array of cylindrical mesopores and is characterised by X-ray diffraction (XRD) values d_{100}, and a_0 the hexagonal unit cell parameter, figure 1.6.

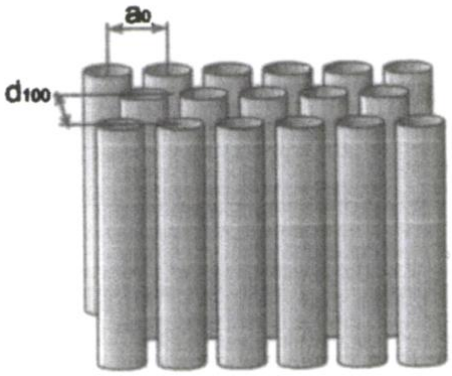

Fig. 1.6: Schematic representation of the structure of hexagonal MCM-41.[42]

The XRD pattern of MCM-41 typically shows three to five reflections between 2θ = 2º and 5º, as in figure 1.7 (a), although samples with more reflections have been reported.[43,44] The reflections are due to the ordered hexagonal array of parallel silica tubes and can be indexed assuming a hexagonal unit cell as (100), (110), (200), (210) and (300). Since the materials are not crystalline at the atomic level, no reflections at higher angles are observed. The XRD pattern of bicontinuous cubic MCM-48 is shown in figure 1.7 (b) and the angles are in the same general region as those for MCM-41 (2-5° 2θ). The most intense peak present is from the (211) while further reflections shown are from (220), (310), (330) and (420). MCM-50, figure 1.7 (c), shows a number of peaks characteristic for a lamellar arrangement i.e. (100) and the higher order (200) and (300) reflections.

It is not possible to quantify the purity of MCM-41 by means of X-ray diffraction alone. Samples with only one distinct reflection have also been found to contain substantial amounts of MCM-41. Corma, 1997, attributed the apparently 'worse' XRD pattern to the formation of smaller, although no less ordered MCM-41 crystallites.[44] In addition, the XRD patterns of MCM-41 containing various degrees of defects were simulated: it was found that even when the hexagonal pore structure

contained a large number of defects, a pattern containing three reflections was found, the same as the hexagonal pattern.[46]

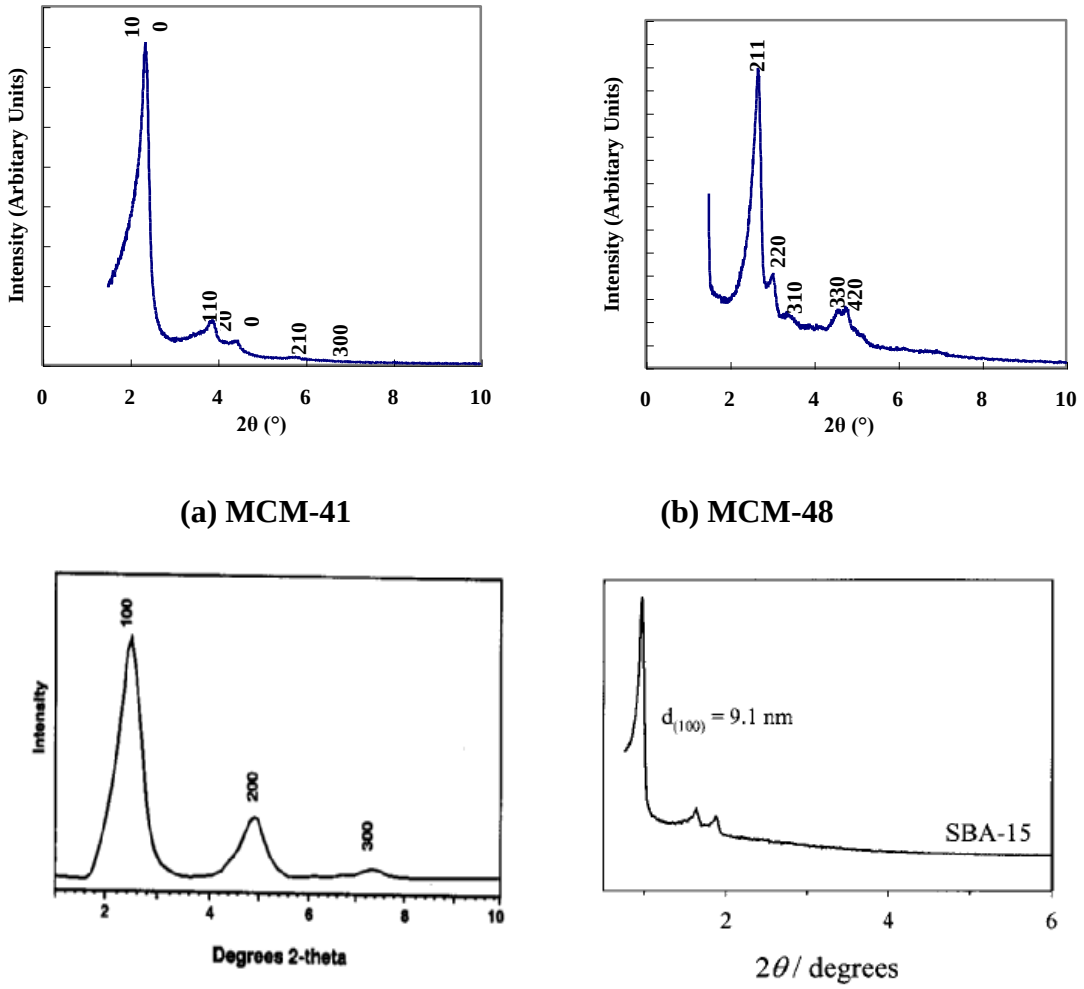

Fig. 1.7: X-ray diffraction patterns for mesoporous silicates.[10,45, 14]

XRD of SBA-15 shows three peaks, a (100) reflection at 0.8-1.1 2θ, the (110) reflection between 1.4-1.6 2θ and a (200) reflection visible at 1.6-1.8 2θ. These reflections, as with MCM are due to the stable pore structure of SBA-15.[14] As with MCM-41 it is not possible to clarify purity of SBA-15 with XRD, however

degradation of a sample can be seen in XRD patterns where the pattern would be clear and visible in the first instance and then not present upon re-analysis.

1.2.3.2: Adsorption Porosimmetry

1.2.3.2.1: Adsorption Isotherms

To gain data from adsorption porosimmetry, adsorption behaviour itself needs to be understood. Adsorption isotherms show the relationship between the volume of gas adsorbed on a solid as a function of applied pressure at a fixed temperature, thereby explaining how a gas adsorbs onto the surface of the solid in question.[47]

Brunauer *et al.* found that the majority of isotherms resulting from physical adsorption can be grouped into five classes, which are shown in figure 1.8.[48] In general, the quantity of adsorbed gas increases with increasing relative pressure (p/p_o, where p_o represents the saturation vapour pressure), and at a certain point the surface coverage corresponds to a monolayer. Further adsorption of gas leads to multilayer adsorption, and finally to a condensed phase.[49]

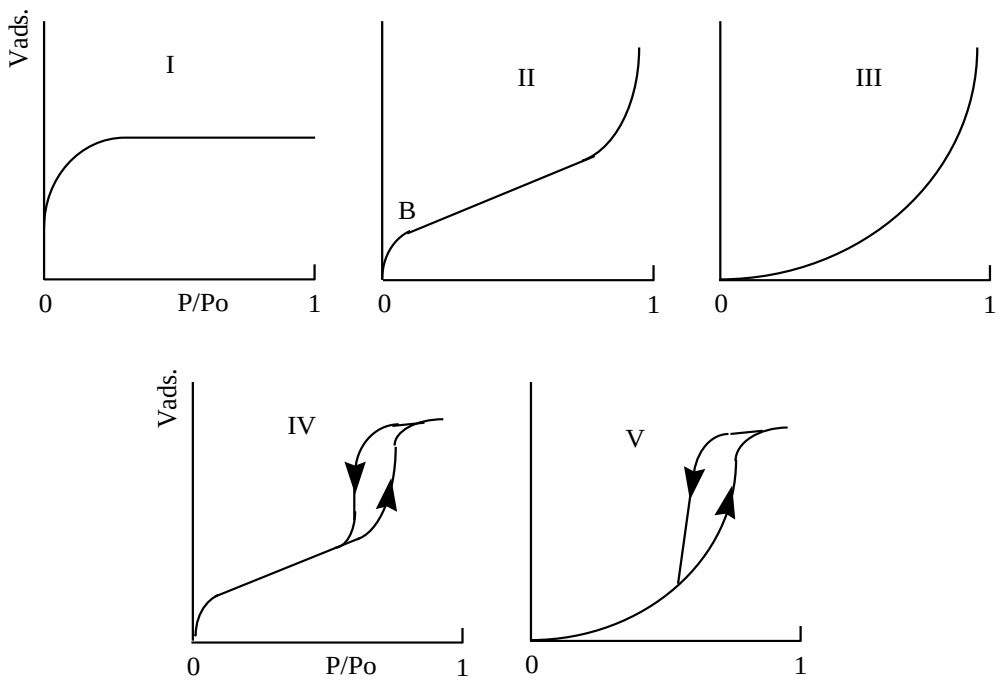

Fig. 1.8: Adsorption isotherms classifications proposed by Brunauer *et al.* [48]

The Type I isotherm is termed a Langmuir isotherm, and corresponds to that expected for reversible adsorption.[48] This isotherm shows a plateau which represents the formation of a monolayer covered surface, and assumes all surface sites are occupied.[50] This response is observed in physisorption for microporous materials, and rarely occurs for non-microporous materials.

The Type II isotherm is encountered for adsorption on non-porous materials and represents unrestricted multilayer adsorption on a heterogeneous substrate.[51] The point of inflection of the curve, (point B in figure 1.8), corresponds to a fully developed monolayer on the solid, while increasing the relative pressure beyond this point results in further adsorption due to the formation of second and higher surface layers.

The shape of the Type III isotherm corresponds to a situation where the attractive forces between the gas molecules are greater than the adsorptive binding forces. Therefore as adsorption proceeds, additional adsorption can occur due to a greater adsorbate interaction for the adsorbed layer than that for the adsorbent surface.

The Type IV response occurs for porous solids, which possess pores in the range 1.5-100 nm. The sharp rise in the volume of gas adsorbed at high relative pressure corresponds to capillary condensation (*Section 1.2.2.3*) of gas in the pores of the solid. The adsorption and desorption branches do not overlap resulting in the presence of a hysteresis loop which can be used to determine the pore size distribution of the solid.

Type V isotherms are similar to type III in the lower relative pressure range, and capillary condensation occurs at higher pressures with an associated degree of hysteresis. Type V isotherms are associated with pores in the same size range as type IV isotherms.

The presence of a hysteresis loop for types IV and V is attributed to the fact that the processes of condensation and evaporation do not occur in an identical manner. This is due to geometrical differences in pore filling and emptying. The IUPAC manual provides a classification for hysteresis loops, and the profiles are illustrated in figure 1.9.

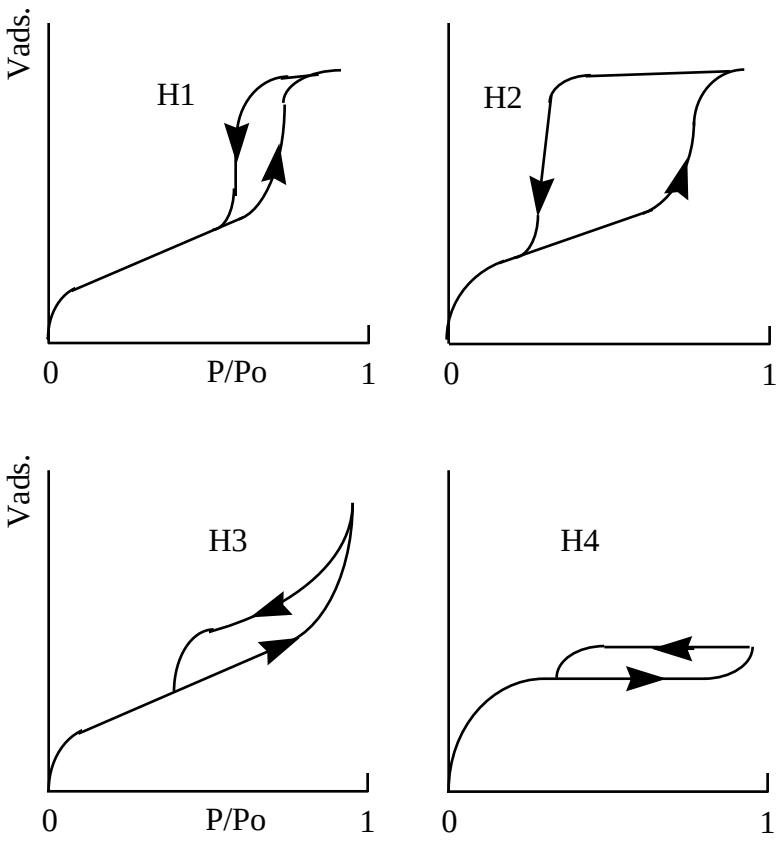

Fig. 1.9: The IUPAC classification of hysteresis loops. [48]

The shapes of hysteresis loops are related to specific pore structures. Type H1 loops are often obtained for agglomerates or compacts of spheroidal particles of fairly uniform size and array. Some corpuscular systems tend to give H2 loops, but the distribution of pore size and shape is not well defined. Types H3 and H4 have been obtained with adsorbents having plate-like particles and slit-shaped pores, respectively.

1.2.3.2.2: Surface Area Calculation from the BET Equation

The volume of adsorbate molecules of known cross-sectional area, required for monolayer coverage, can be used to determine the surface area of a solid. The isotherm derived by Brunauer, Emmett, and Teller (BET) is essentially a

generalisation of Langmuir's treatment for monolayer coverage applied to multilayer adsorption.[52] The basis for this theoretical treatment is that the first layer of adsorbed molecules serves as a site for the adsorption of a molecule to form the second layer, and so on. The usual form of the equation derived by Brunauer *et al.* is shown in equation 1.2

$$\frac{p}{n(p_o - p)} = \frac{C_{BET} - 1}{n_m C_{BET}} . \frac{p}{p_o} + \frac{1}{n_m C_{BET}} \qquad \textbf{Eqn. 1.2}^{[52]}$$

where n = the number of moles adsorbed at pressure p

n_m = the number of moles required for monolayer coverage, and

C_{BET} = a constant for a given adsorbent

The value of C_{BET} is most frequently between 50 and 300 when using Nitrogen as an absorbate. A lower value of C_{BET} is an indicator of a low heat of adsorption producing a type I isotherm, shown in fig 1.8. High C_{BET} values show a type II isotherm, and for a C_{BET} value of less than 2 a type III isotherm is formed.[53]

The constant C_{BET} is coupled exponentially to the heats of adsorption (ΔH_1) and condensation (ΔH_C) of the gas:[49]

$$C_{BET} = \Psi \exp\left[(\Delta Hc - \Delta H_1)/RT\right] \qquad \textbf{Eqn. 1.3}$$

where Ψ is the ratio of internal degrees of freedom in a molecule of the monolayer (j_m) and of the condensed phase (j_c).

A plot of $\{p/[n\,(p_0-p)]\}$ versus p/p_0 should produce a straight line with a slope equal to $\{(C_{BET}-1)/n_mC_{BET}\}$ and an intercept of $1/n_mC_{BET}$. This enables the total surface area to be calculated using equation 1.4

$$S_{BET} = \frac{n_m N A}{V_m} \qquad \textbf{Eqn. 1.4}$$

where S_{BET} = the BET surface area

N = Avogadro's number (6.023×10^{23} molecules mol^{-1})

A = surface area occupied by one gas molecule (0.162 nm^2 for N_2)

V_m = molar gas volume at STP (22.4 dm^3mol^{-1})

The BET theory is primarily applicable for a relative pressure range of 0.05 to 0.3, and C_{BET} values between 80 and 120, generally type II isotherms. A number of assumptions are implicit in the BET model.[47,54]

a) One questionable assumption is that of an energetically homogenous surface. Experimental evidence from curves of heat of adsorption as a function of the quantity adsorbed illustrate that the deviation from homogeneity can be quite considerable.

b) The model also ignores the influence of lateral adsorbate interactions. It is certain that adsorbate-adsorbate interactions must be far from negligible when a layer is nearing completion.

c) Further criticism arises from the question of how far the molecules in all layers after the first layer should be treated as completely equivalent, as the adsorbate-adsorbent interaction diminishes significantly as the distance from the surface increases.

1.2.3.2.3: Capillary Condensation

Zsigmondy proposed a theory for capillary condensation on the basis that the equilibrium vapour pressure, *p*, over a concave meniscus of liquid, must be less than the saturated vapour pressure, p_0, at the same temperature.[55] This fact implies that a vapour can condense to a liquid in the pores of a solid, even when its relative pressure is less than one. Zsigmondy's model assumes that initially, at low relative pressures, adsorption is restricted to a thin layer on the walls, until capillary condensation commences in the finest pores at the point of origin of the hysteresis loop. As the pressure is increased, progressively larger pores are filled (figure 1.10), until the system is considered to be full of condensate at the saturation pressure.

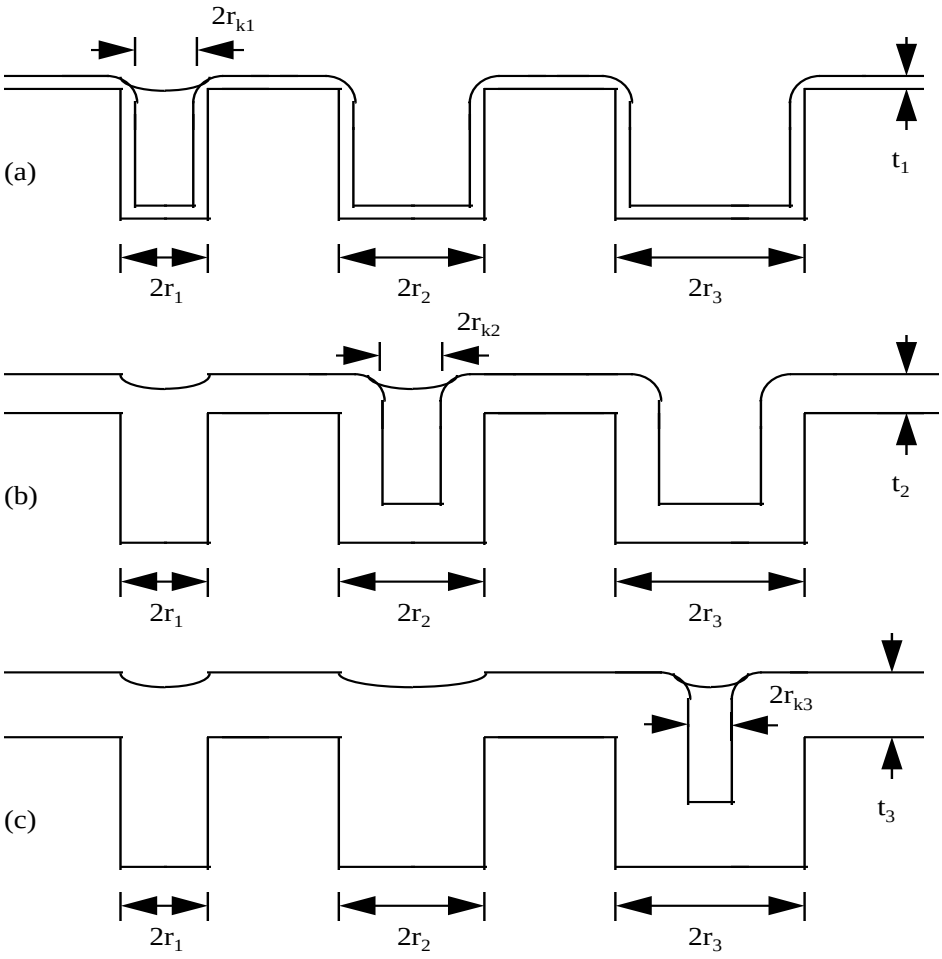

Fig. 1.10: Multilayer physisorption and capillary condensation processes within pores at (a) low, (b) medium, and (c) high relative pressure values.

It was subsequently assumed that the pores were cylindrical with a contact angle of zero, so the meniscus was hemispherical. The mean radius of curvature therefore equals the radius of the pores less the thickness of the adsorbed film on the walls. Hence it is possible to determine the mean radius of pores in which capillary condensation can occur, using the value of the relative pressure at the lower limit of the hysteresis loop, from the Kelvin equation (equation 1.5).[54]

$$r_k = \frac{-2V\gamma\cos\theta}{\ln(p/p_o)RT} \qquad \textbf{Eqn. 1.5}^{[54]}$$

where r_k = Kelvin radius

γ = adsorbate surface tension

V = adsorbate molar volume

θ = adsorbate-surface contact angle.

For nitrogen adsorbate at 77K:

$$r_k = \frac{0.415}{\log(p_o/p)} \qquad \textbf{Eqn. 1.6}$$

1.2.3.2.4: BJH Method for Mesopore Size Distribution

Multilayer physisorption and capillary condensation occur in mesopores at relative pressure (p/p_0) greater than approximately 0.3. When determining the range of mesopores within a solid, the mesopore radius is therefore the sum of the radii derived

from both processes. This is the basis for the Barrett-Joyner-Halenda (BJH) method for mesopore size distribution determination.[56,57]

The pore radius resulting from multilayer physisorption, r_t, can be determined using a graphical procedure known as the MP method, and that due to capillary condensation, r_k, evaluated using the Kelvin equation (equation 1.6).[54] The MP method uses values of the statistical thickness, *t*, defined as the thickness of the adsorbed film on a pore wall, to calculate pore dimensions.

The values of *t* were originally calculated from analysis of non-porous solids and for a specific analysis, *t* is determined from relative pressures p/p_o and the C_{BET} value, i.e. partial pressures are converted to values of *t*.[54] The volume of gas adsorbed *V* is then plotted versus *t* giving a *t-plot* or *V-t curve* figure 1.11. Curve X results from multilayer adsorption in the absence of condensation into pores while curve Y shows an upward deviation from linearity. The downward deviations from linearity result when pores are filled by multilayer adsorption and these values are used in the MP method to evaluate the micropore volume over a given statistical thickness range. A pore size distribution can be calculated by differentiating the *V-t* curve where the differential pore volume is plotted versus the pore radius r_t (calculated as the average of two successive *t* values).

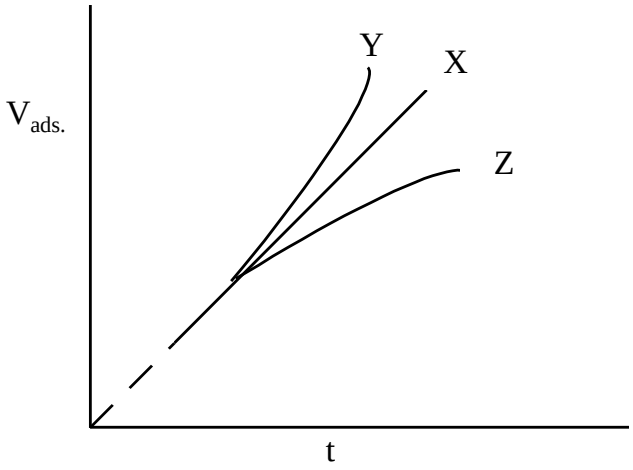

Fig. 1.11: A typical V-t curve.

In the BJH method a particular pore shape is assumed, and r_t and r_k are summed to give the actual pore radius r. The adsorbate liquid volume (determined from the corresponding values of n, the quantity of gas adsorbed) from the isotherm is plotted versus r to give a cumulative pore size distribution and differentiated giving the differential pore volume distribution as a function of pore diameter i.e. pore size distribution.

1.2.3.2.5: Porosity Analysis of Mesoporous Silicates

Adsorption of probe molecules has been widely used to determine the surface area and to characterise the pore size distribution of mesoporous materials. Soon after the preparation of MCM materials, the physisorption of gases such as N_2, O_2 and Ar had been studied to characterise the porosity.[58-61]

The nitrogen adsorption isotherm for MCM-41 with pore diameter approximately 4.0 nm, which is type IV in the IUPAC classification, shows two distinct features: a sharp capillary condensation step at a relative pressure of 0.4 and the absence of hysteresis between the adsorption and desorption branches (figure 1.11). The adsorption at very

low relative pressures, p/p_o, is due to monolayer adsorption of N_2 on the walls of the mesopores and does not represent the presence of any micropores.[62,63]

However, in the case of materials with pores larger than 4.0 nm or using O_2 or Ar as adsorbate, the isotherm is still type IV but also exhibits well-defined hysteresis loops of the HI type.[48,59,64] The presence and size of the hysteresis loops depend on the adsorbate, pore size and temperature.[59,64,65] Non-local density functional theory (NLDFT) provides an accurate description of the thermodynamics of nitrogen confined in pores of this size and predicts the thermodynamic limits for the adsorption-desorption hysteresis loops.[66]

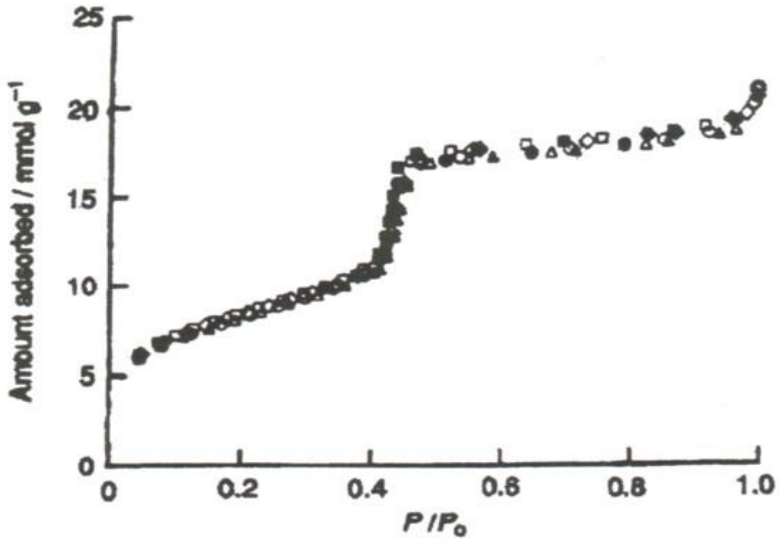

Fig. 1.12: Nitrogen adsorption isotherm of MCM-41 at 77K.[66]

Comparison of the theoretically predicted thermodynamic hysteresis loops with experimental data on MCM-41 supports the classical physical scenario of capillary condensation in an open cylindrical capillary. In contrast, there is still no clear explanation for those cases where the hysteresis loops are absent. Calculations by

Ravikovitch *et al*. showed that the absence cannot be explained by the capillary critical temperature being achieved, which was previously assumed.[63,66,67]

To determine the pore size distributions in cylindrical pores, several methods are known based on geometrical considerations, thermodynamics or a statistical thermodynamic approach.[54,66,68] The BJH method is based on the Kelvin equation and thus has a thermodynamic origin. The pore size distribution of MCM-41 calculated using the BJH method is shown in figure 1.13.[56,57]

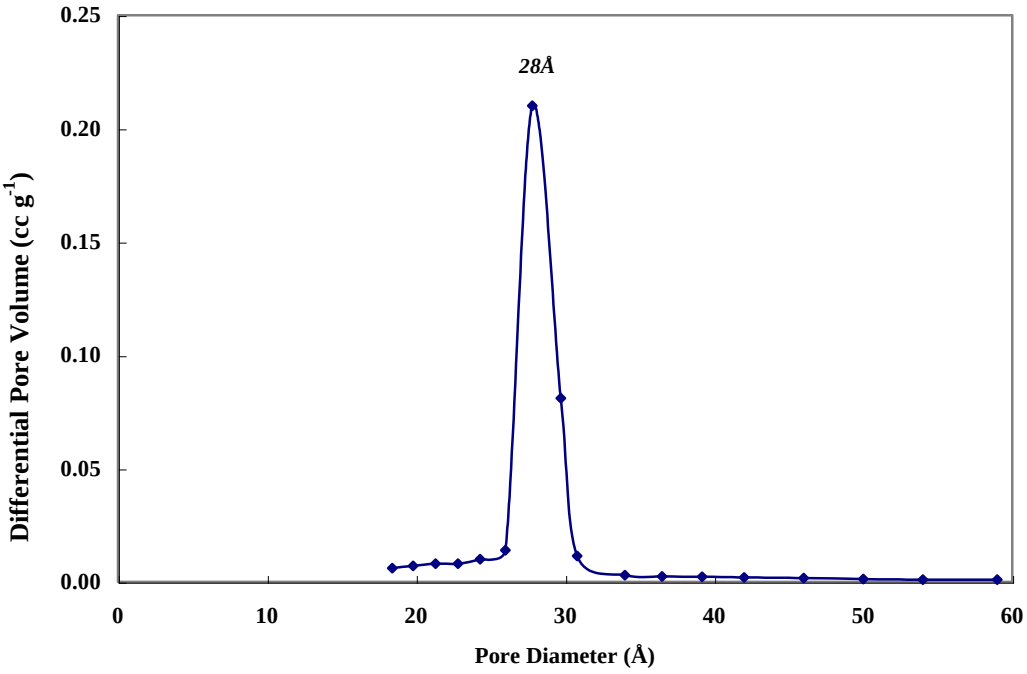

Fig. 1.13: BJH pore size distribution of MCM-41[45]

1.2.3.3: Transmission Electron Microscopy (TEM)

Transmission electron microscopy (TEM) is used to elucidate the structure of mesoporous materials. In TEM, a sample is prepared, crushed and placed in a thin layer, <1000nm, on a carbon foil. For materials where the majority of the detail and characteristics are internal, this is a very useful and powerful technique. Figure 1.14

shows a TEM image of the hexagonal arrangement of uniform pores in a mesoporous sample. However, the exact analysis of pore sizes and thickness of the pore walls is very difficult and not possible without additional simulations because of problems with focussing at the high magnifications involved.

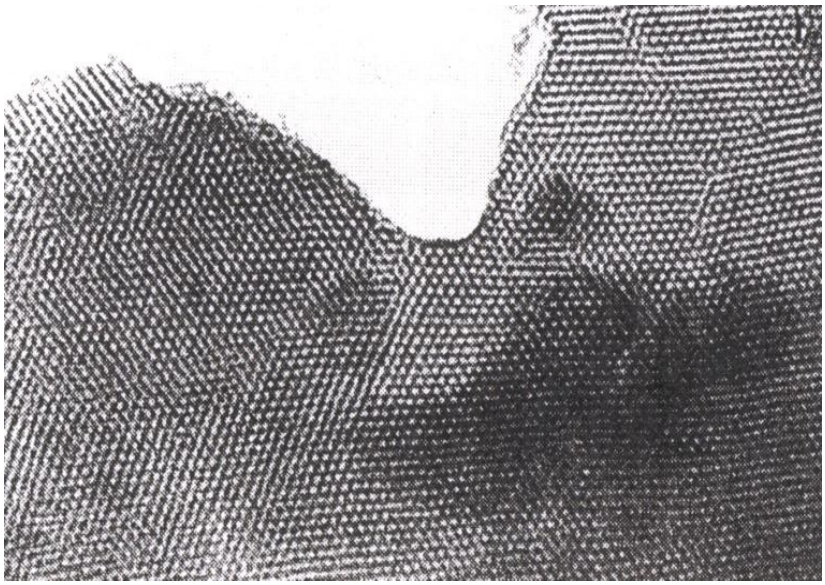

Fig. 1.14: Transmission electron micrograph of calcined zirconium oxo phosphate showing a hexagonal pore arrangement analogous to MCM-41 materials (scale bar not shown).[69]

It was shown by Chen *et al*. that, for MCM-41, the thickness of the features (pore size and wall thicknesses) depend strongly on the focus conditions, and careful modelling is necessary for a precise analysis.[70] Moreover, most MCM-41 samples not only show ordered regions but also disordered regions, lamellar (prior to calcination) and fingerprint-like structures.[71] Chenite *et al*. showed that the equidistant parallel lines observed in the micrographs are related to the hexagonal

repeat between tubules.[72] The honeycomb structure is sufficiently regular to give fringes in projection under proper orientation of the specimen. Feng *et al*. investigated the curved, fingerprint-like structures in more detail, and observed two dislocation and two disclination defect structures, which are similar to those detected in pure liquid-crystal phases.[73] Using TEM imaging as a basis for their conclusions, they proposed that since the mesoporous structure cannot shear without fracturing, these defects must have formed in the unpolymerised liquid-crystal like silicate precursor phase.

TEM's use with SBA-15 has become widespread as a technique in analysing SBA-15 structure and the effects of changes in the sample preparation and treatment. [14,74-76]

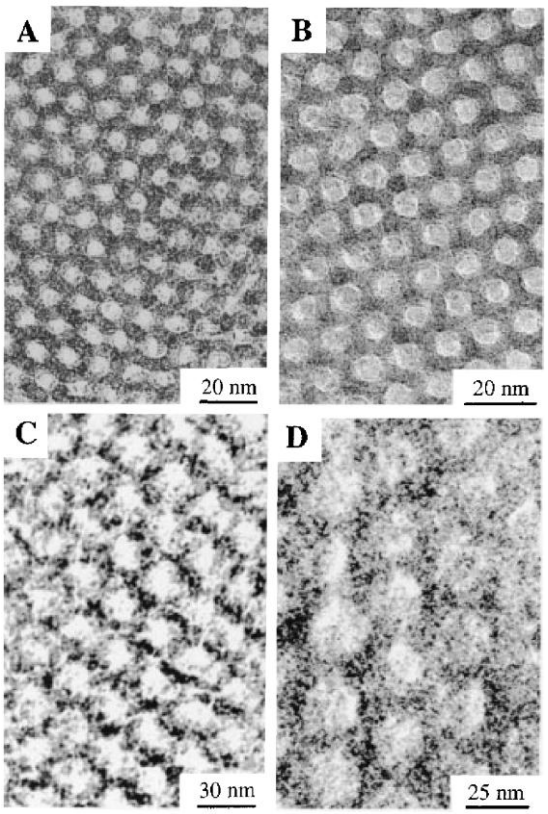

Fig 1.15: TEM images of SBA-15 with average pore sized (a) 60 Å (b) 89 Å (c) 200 Å (d) 260 Å[14]

The images in figure 1.15 show clearly the ordered honeycomb structure of SBA-15 with differing average pore size. SEM however, has been the preferred tool for microscopy of SBA-15.

1.2.3.4: Scanning Electron Microscopy (SEM)

Scanning Electron Microscopy allows a greater depth of field than TEM and allows the user to determine the surface structure of materials to the nanometer (nm) and micrometer (μm) scale.[77]

Figure 1.16 below shows how useful the technique is in looking at mesoporous oxides in the nm and μm scale.

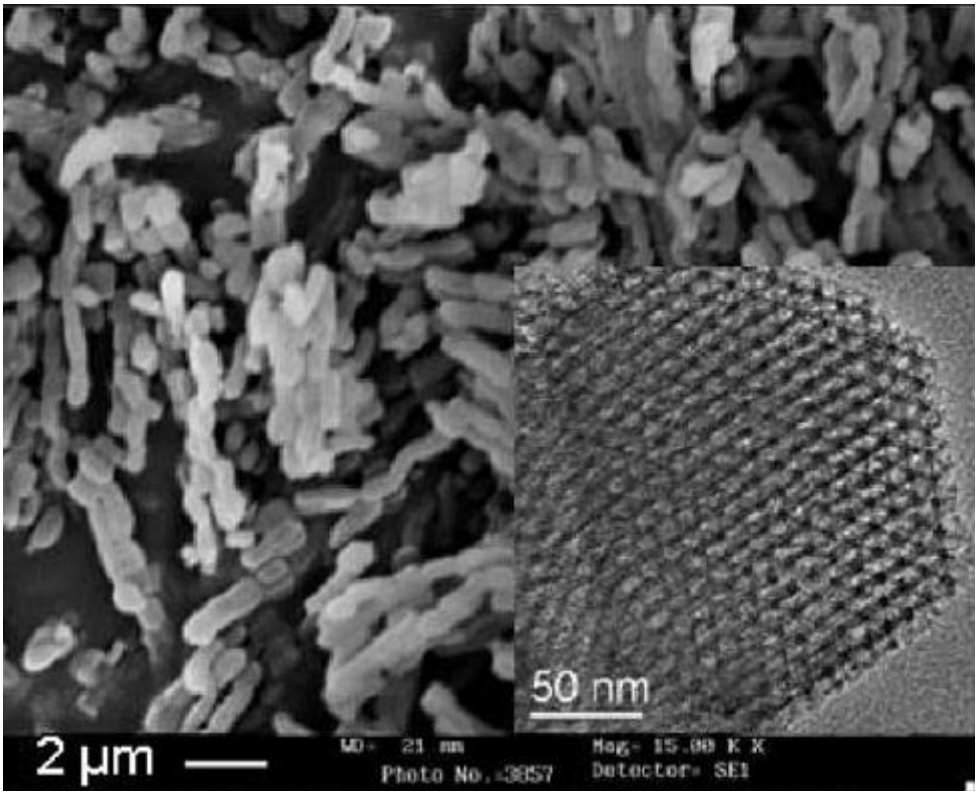

Fig 1.16: SEM images of SBA-15 [78]

SEM is a very popular technique, this is due in the main to the capability of the technique to obtain images that are three dimensional in character for the surfaces of materials.[77] SEM works by directing a beam of electrons from an electron gun at the top of the microscope in a vertical path to the sample. This is done in a vacuum in order to ensure the electron beam reaches the sample rather than scatters of gaseous species within the microscope. The electron beam is focussed through lenses and electromagnetic fields and finally hits the sample. When the electron beam impinges on the sample, the sample emits secondary electrons and X-Rays from the surface structure. These are then detected and converted into an image for display. (Fig 1.17) shows the full set up of a standard SEM.

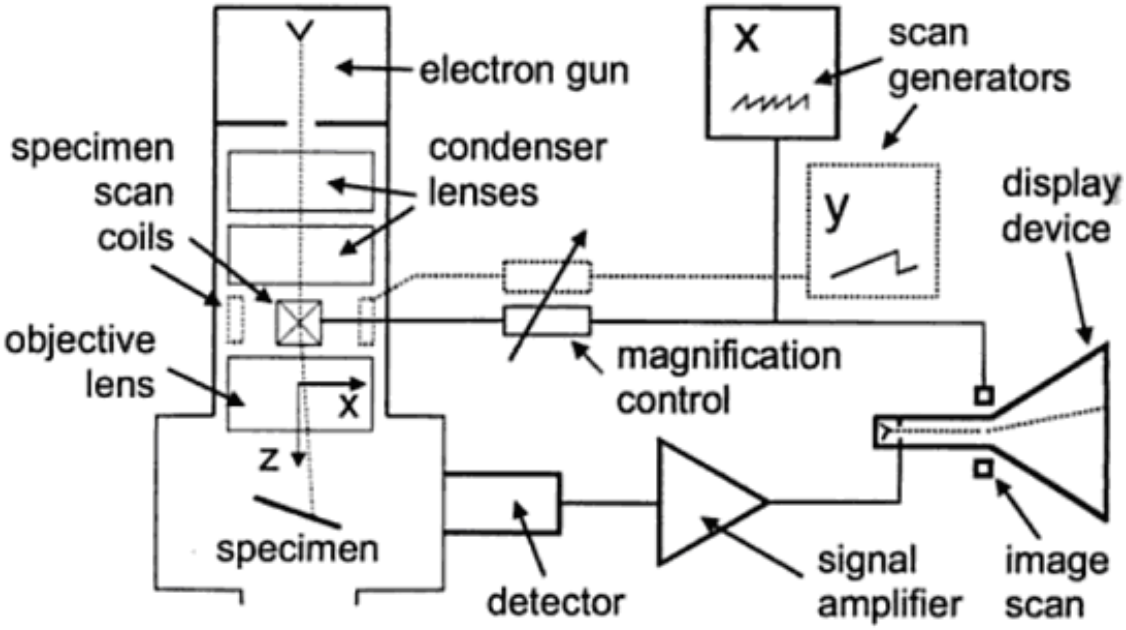

Fig 1.17: Schematic diagram of a scanning electron microscope.[79]

1.3: Allotropes of Carbon

Carbon is the lightest group VI element and is the most interesting due to its tendency to form different allotropes, diamond, graphite and fullerene are the most well known of these.

1.3.1: Hybridisation

The chemical bonding of different allotropes of carbon depends upon the hybridization of the *s* and *p* orbitals. Hybridisation is the generation of a new set of atomic orbitals, hybrid orbitals, by the combining of atomic orbitals in an atom. Hybrid orbitals are the atomic orbitals produced when two or more nonequivalent orbitals of the same atom combine. Within carbon these hybrid orbitals are formed when the s and p orbitals combine. The hybrid orbitals form covalent bonds and, with carbon, can form a maximum of four sp^3 orbitals (figure 1.18), three sp^2 orbitals (figure 1.19) and two *sp* orbitals (figure 1.20).

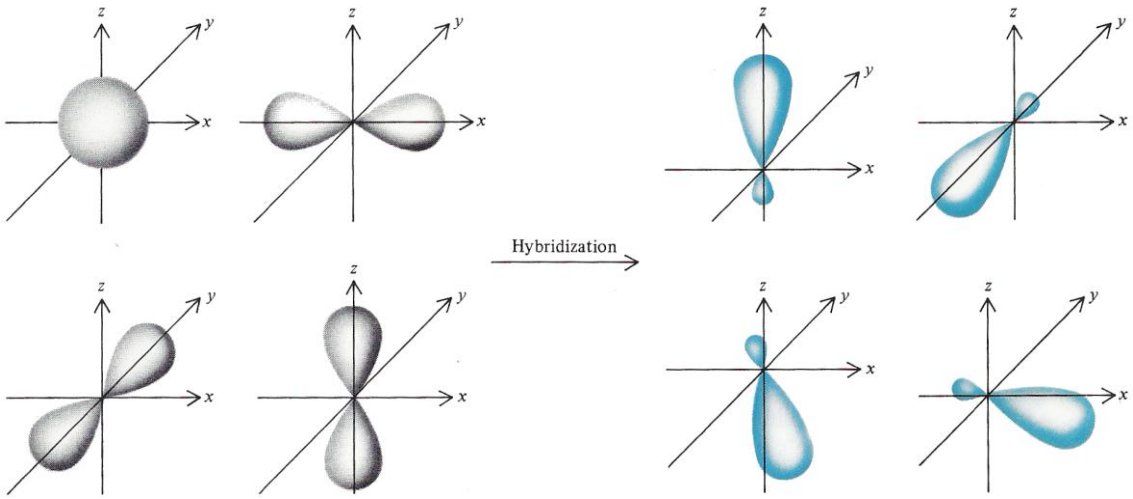

Fig 1.18: The structural rearrangement of *s* and *p* orbitals to form four hybrid sp^3 orbitals.[80]

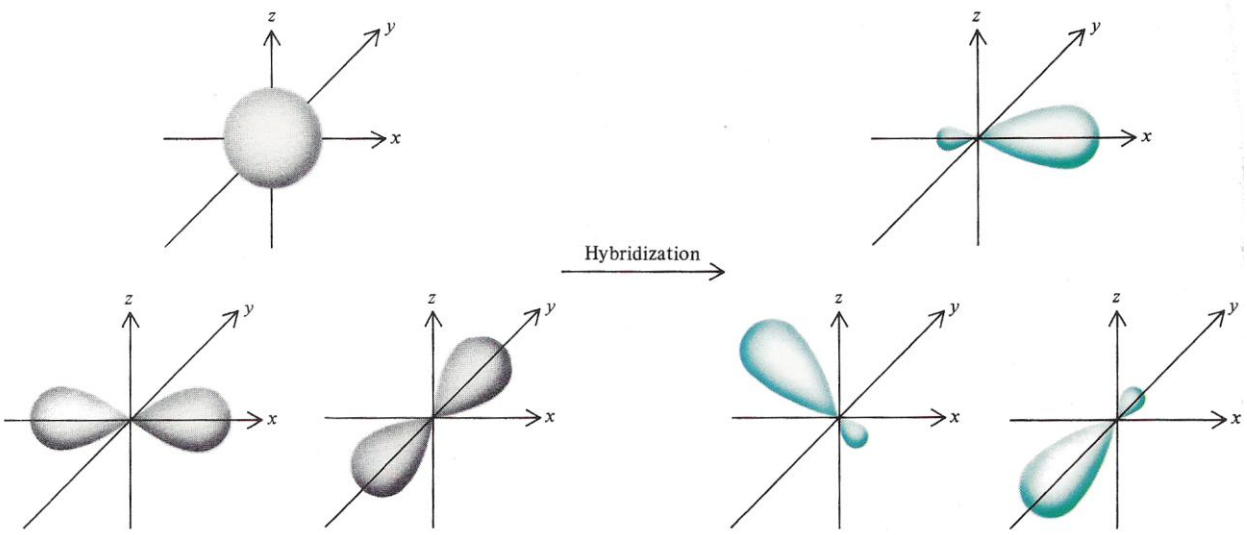

Fig 1.19: The structural rearrangement of *s* and *p* orbitals to form three hybrid sp^2 orbitals. [80]

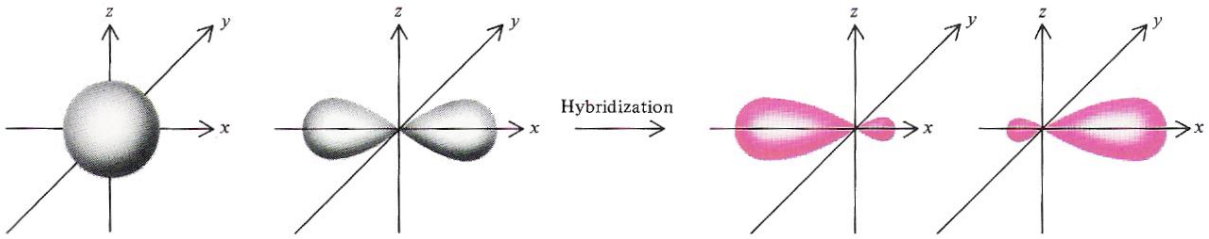

Fig 1.20: The structural rearrangement of *s* and *p* orbitals to form two hybrid *sp* orbitals. [80]

Table 1.2 below shows the effect hybridization of atomic orbitals has on the structure, and consequently the allotrope of carbon that is formed.

Typical Chemical Bonding					
Physical Dimensionality and coordination number (z)	Hybridization	Bond Length (Å)	Energy (eV $mole^{-1}$)	Solid state phases	Shape of hybrid orbitals
3D (tetrahedral structures $z = 4$)	sp^3-sp^3	1.54	15	Diamonds	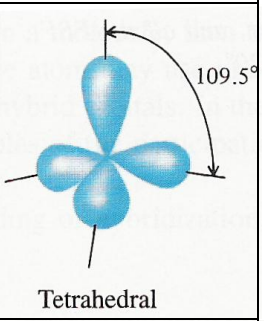
2D (lamellar Structures $z = 3$)	*aro-aro*	1.40	25	Graphites (plane surfaces)	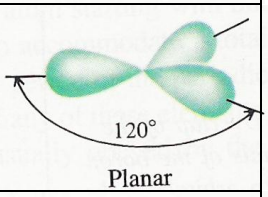
	sp^2-sp^2	1.33	26.5	Fullerenes (curved surfaces)	
1D (Chains or rings $z = 2$)	sp^1-sp^1	1.21	35	Carbynes	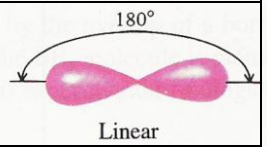

Table 1.2: A table showing bonding properties within allotropes of carbon. [80,81]

1.3.2: Graphite Structure

Graphite is an allotrope of carbon with sp^2 hybridised aromatic covalent bonding, the structure of graphite, shown in figure 1.21, is therefore two dimensional and planar. When the overall structure of graphite is examined in 3D, the 2D layers are separated by 3.35Å, much larger than the C-C bond distance of 1.42Å.[81] Graphite has lubricating properties due atomic adsorption of water vapour within the layers and, because of weak interplanar forces allowing the movement of the 2D planar structures over one another. [82]

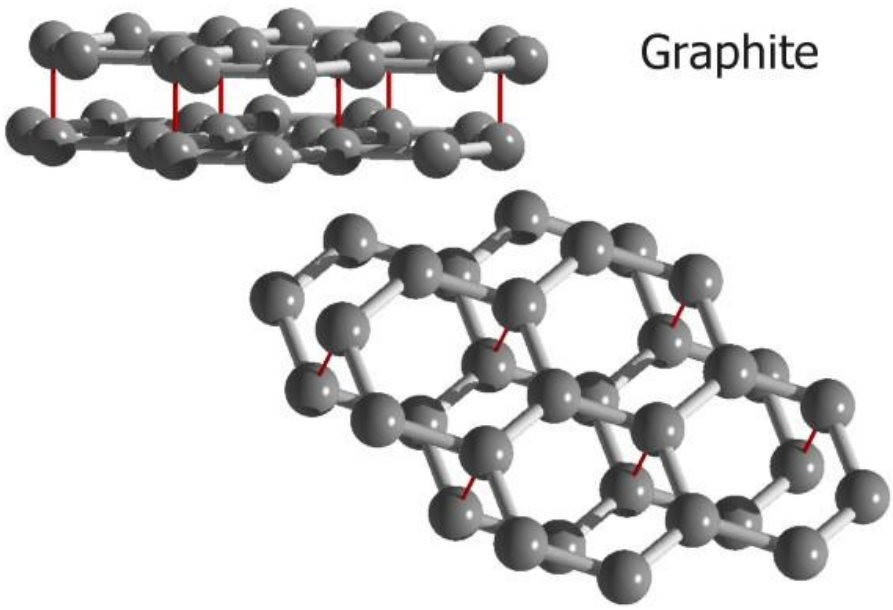

Fig 1.21: Structure of graphite planar and top view, the red lines depict weak interplanar forces. [83]

1.3.3: Fullerene Structure

Fullerenes, as graphite, are sp^2 hybridised, however, their structure is not planar, the bonding is such that fullerenes create spheroids. Buckminster fullerene, C60, shown here in Fig 1.22, is probably the most well known fullerene, discovered in 1985 it was the catalyst for further fullerene research.[84]

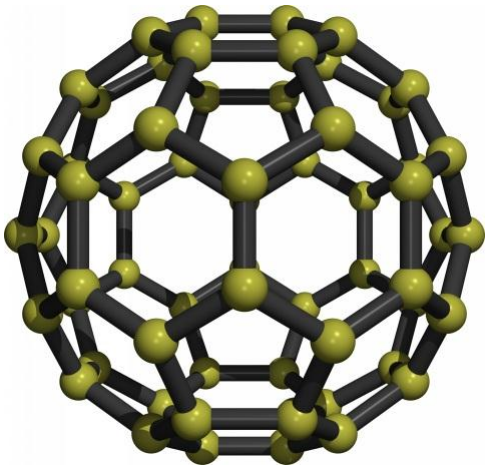

Fig 1.22: Buckminster fullerene carbon structure discovered in 1985. [85]

Fullerenes are usually formed by the clustering of carbon through laser vaporization of graphite, however this approach yields a range of cluster sizes, typically clusters from 10 to 18 atoms, and 32 to 60 atoms in size. [86,87] It is believed that these fullerenes grow by the addition of carbon atoms, much like the paving in a road, leading to the process being nicknamed the "fullerene road". [88,89] Fullerenes in general have a wide range of structures, more common structures are shown here in fig 1.23. The smallest of which that is known to be stable is C_{20}, and the largest that has so far been reported are between C_{600} and C_{700}. [81,90]

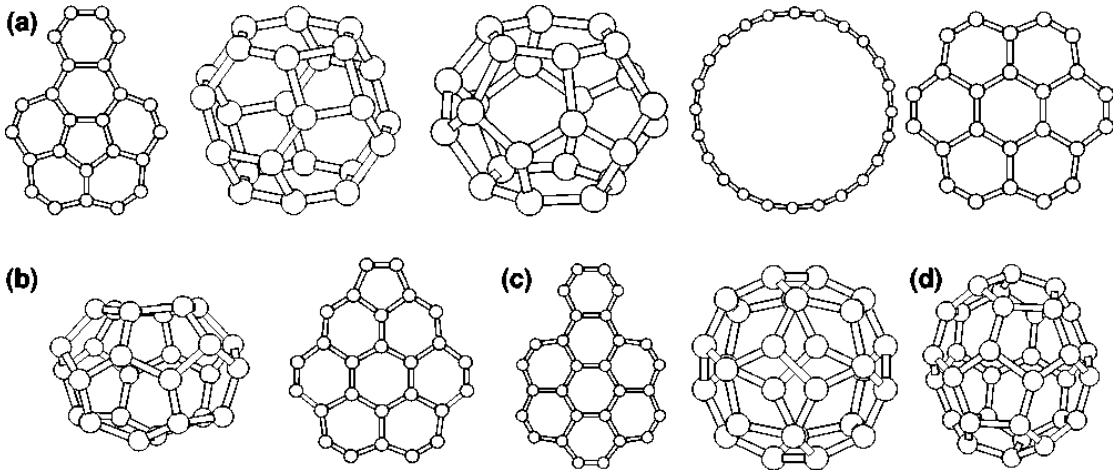

Fig 1.23: Common structures of the C*n* clusters. a) C24 one-pentagon bowl, *Oh* cage, *D*6 fullerene, ring, and sheet, (b) C26 fullerene and one-pentagon sheet (c) C28 sheet and fullerene (d) C32 fullerene. [91]

Buckeyballs are extremely strong molecules, they can withstand pressures of over 3,000 atmospheres and still bounce back to their original shape. [92] However, they do not bond together chemically, this gives them potential as a lubricant, however, the molecules tend to be too small for many applications as they become lodged in crevaces.[92]Fullerenes are also used as precursors for materials such as diamond

coatings or nanotubes. These fullerene nanotubes are sought after as they have the same ability to withstand the high pressures and still return to their original shape.[92]

1.3.4: Diamond Structure

Diamond has a lattice structure, with two interpenetrating face-centered cubic lattices. Each lattice is one quarter of a lattice constant apart from the other, and is tetrahedrally arranged with four other carbon atoms in the sublattice, as shown in Fig 1.24. It is this structure which is responsible for the very strong carbon–carbon bonding, which in itself, results in its properties such as extreme high hardness, extremely high thermal conductivity, and chemical inertness.[93–94] It is for these properties that metastable diamond is sought after as a material for many applications.[95–107]

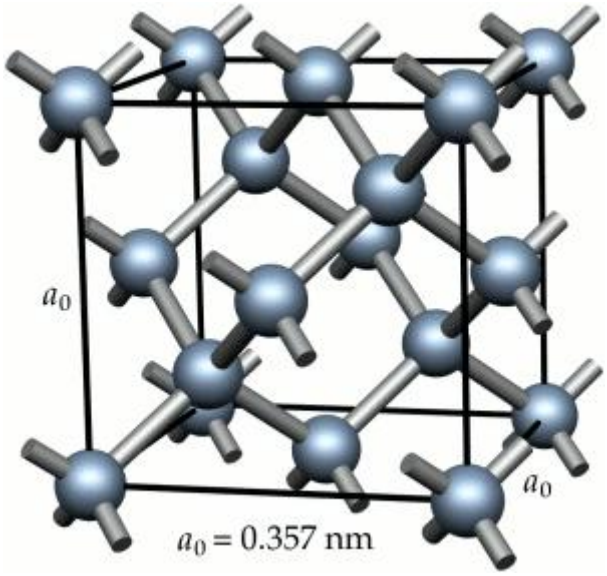

Fig. 1.24: Structural framework of diamond, showing the interconnecting lattices.[108]

This demand for metastable diamond has driven researchers to look into methods of creating diamond, especially since the first reported synthesized diamonds using a high-pressure and high-temperature process (HPHT). [109,110] There are now many

different routes, through which diamond synthesis can be achieved, in addition to the original HPHT synthesis, Chemical Vapour Deposition (CVD) has become widely used to grow metastable diamond. [101,111]

1.4: Chemical Vapour Deposition (CVD)

1.4.1: CVD Technique

CVD is a process where a volatile precursor gas comes into contact with a heated substrate causing a reaction and depositing a thin solid film onto the substrate. [112] It involves a chemical reaction in the gas phase, which occurs above a solid deposition substrate surface. All techniques of CVD use gas phase reactions to propagate the growth of the solid films that are wanted from the experiment, as illustrated in figure 1.25.

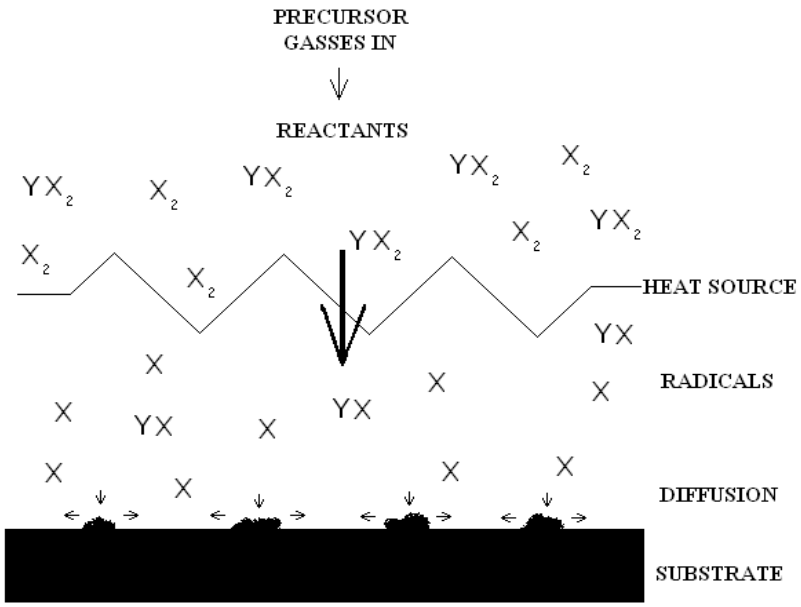

Fig 1.25: Schematic diagram of CVD using precursor gasses to form radicals that can diffuse onto the substrate surface, leaving a solid film. (adapted from Ashfold et. al.)[113]

There are three main types of CVD activation process used for diamond growth, namely, hot filament, plasma and torch CVD. They are all similar in the fact that the initiating reaction that occurs is in the gas phase above the deposition surface; however, the methods of inducing this reaction differ completely. The input gas mixture is usually a hydrocarbon gas diluted in hydrogen (most commonly 1% CH_4-H_2).

1.4.1.1: Hot Filament CVD

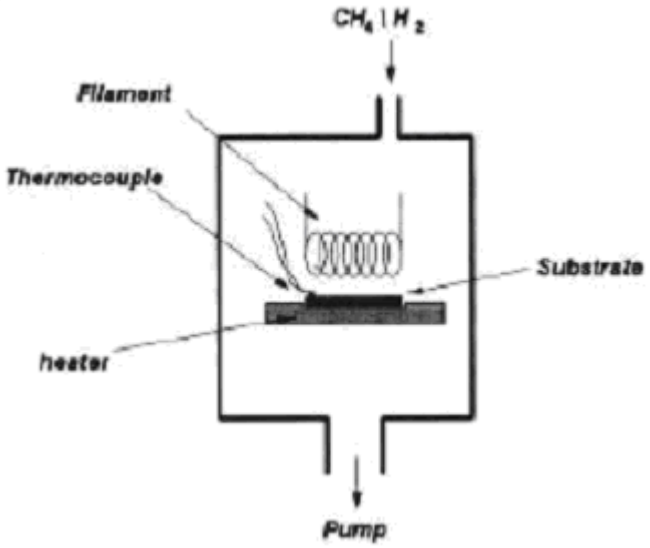

Fig 1.26: Schematic diagram of Hot Filament CVD apparatus. [113]

In 1982, Matsumoto first published the process of hot filament CVD, where he used a low pressure vacuum, achieved with a rotary pump.[114] The precursor gasses are in a constant flow over the filament at ≈2200K and between 2-8mm from the substrate. Catalytic dissociation of the precursor gas species occurs at the filament to produce reactive species, such as atoms and radicals, which cause deposition. Within this kind of CVD chamber the walls are preferentially cooled, thus limiting the CVD film or crystal growth in all places other than on the substrate. This happens because most

CVD reactions are endothermic, absorbing heat, the implication of this is that the sample will preferentially grow on the substrate where the temperature is higher and leave the cool walls of the chamber uncoated. Diamond film growth rates of ~1μm/hr are typically achieved by HFCVD. [115]

1.4.1.2 Microwave plasma CVD

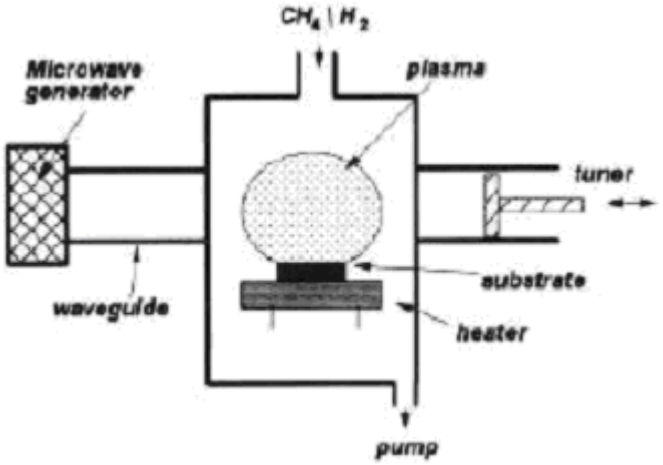

Fig 1.27: Schematic diagram of a Microwave Plasma CVD reactor. [113]

A Microwave plasma induced CVD set up can be achieved by the proper combination of electric and magnetic fields.[116, 117] As with hot filament CVD, microwave plasma CVD is conducted at low pressure.[118] The microwave plasma induces ionisation of gasses, forming highly energetic electrons and lower energy, higher mass, ions. The high energy electrons collide with gas molecules resulting in dissociation of the molecules and the formation of highly reactive chemical species which begin the deposition reaction. Growth rates of diamond scale almost linearly with power of the microwave generator, a 1kW plasma produces growth rates of ~1μm/hr. [115]

1.4.1.3 Oxyacetylene Torch CVD

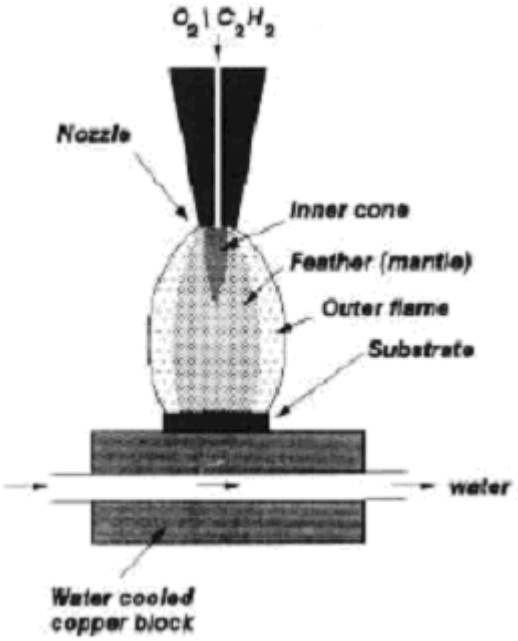

Fig 1.28: Schematic diagram of Oxyacetylene Torch CVD. [113]

The oxyacetylene torch was first used as a method of CVD in 1988 by Hirose.[119] This method of CVD has potential been seen in further experiments as one of the major successes of the diamond CVD techniques.[116, 120] In this technique, excess fuel and CO are oxidised whilst hydrogen and acetylene are burned. Diamond forms on a substrate at a rate of 100-200 micrometers per hour and a temperature of 800-1100^{o}C.[121] The reason this technique is seen as an important prospect in Diamond CVD growth is because of these high growth rates, however as yet, the Diamond formed from this technique is not uniform in structure.[121]

1.4.2 CVD Growth of Diamond

Diamond CVD utilises standard CVD techniques, however the precursor gasses are limited to substances which contain only carbon and hydrogen and also Nobel gasses. Using these gasses, the growth of diamond can be achieved on diamond or silica substrates. The growth of diamond on these substrates is seen in the same orientation as the substrate and often can be layered.[116, 122-124]

CVD growth of Diamond usually takes place following five stages, firstly, incubation, where the initial nucleation occurs. Secondly, nucleation of individual crystals, in this stage the nuclei of diamond become available for larger nucleation of individual diamond crystals. Thirdly, the termination of the surface nucleation, during which there is growth of individual crystals. In the fourth stage we can see the formation of a continuous film of diamond, of which the growth is the fifth stage.[125]

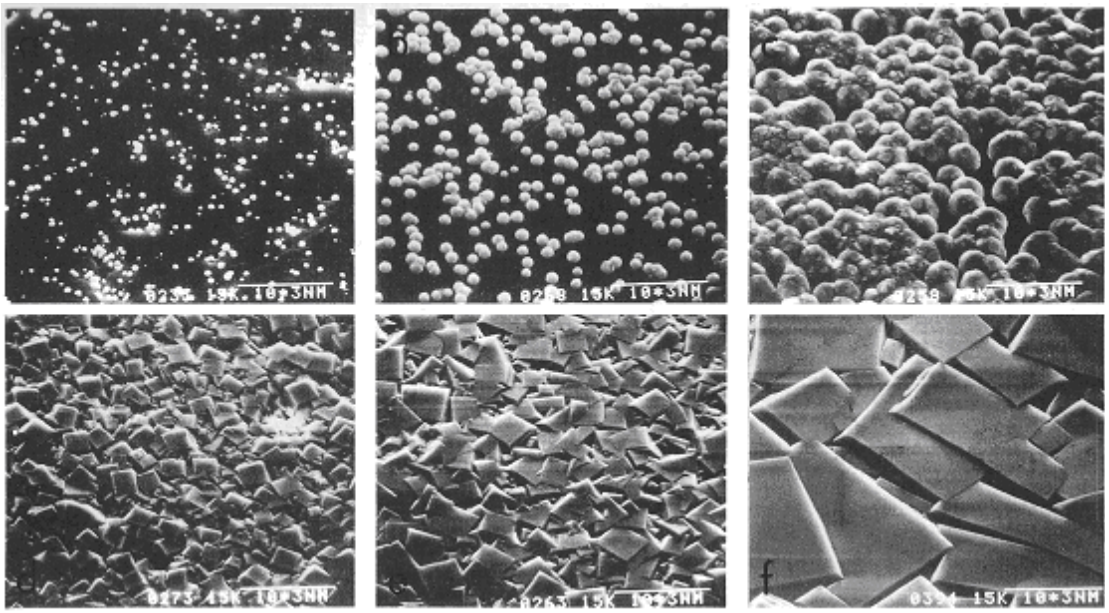

Fig 1.29: Growth process of a diamond film. (top left) nucleation, (centre top) termination of nucleation, (top right) growth of individual crystallites, (lower three images) continuous film growth. [116]

Depending on the substrate material, the incubation period can take from a few minutes to hours. The nucleation during this time can be seen in figure 1.29 and the process of nucleation has been previously shown in figure 1.25, as the radical or ionised gasses diffuse from the filament the diamond will nucleate upon the substrate.[116] On an atomic scale, there are six processes which may be seen during surface nucleation.[116] These are:

1- Atoms impinge upon the deposition substrate from the gas phase and become absorbed onto the surface.

2- The adatoms may desorb or diffuse over the surface. The adatoms may also diffuse into the substrate or bond to other surface atoms.

3- With increasing time, the surface concentration of the adatoms increases and clusters form.

4- Through Statistical fluctuation in the local adatom concentration, the clusters either grow or decay.

5- There exists a critical size above which the probability of growth will be greater than decay, so that the clusters with a size exceeding the critical size become stable.

6- The stable clusters provide suitable growth sites for growth, both from migratory adatoms and from the atoms in the gas phase.

After these initial clusters are formed, nucleation of individual crystals takes place. At first, these crystals are amorphous, however as the process moves through the third stage, termination of nucleation into the fourth stage, the growth of a film, the crystals begin to arrange themselves to achieve the lowest surface energy for a diamond

crystal.[126,127] It is from this ordered layer growth where the final step, growth of a single crystalline film occurs.

1.5 Diamond Nanorods

Rods of diamond have been produced since 1968 when diamond whiskers were grown using a vapour-liquid-solid mechanism.[128] This is where a liquid phase catalyst alloy rapidly absorbs a gas vapour to levels where it is supersaturated and crystal growth then occurs from nucleation sites.[129] Further work on diamond nanorods between 1968 and 2004 was slow in progress due to the difficulty in producing good quality nanorods.[130]

In 2000, progress was made when aligned diamond whiskers with small diameters ~60nm were synthesised.[131] This was achieved, not by chemical vapour deposition growth, but rather by air plasma etching of polycrystalline films using Molybdenum as a mask to prevent etching of the wires. This molybdenum makes the diamond nanorods impure and their theoretical electronic properties would become inhibited, making the nanorod produced less desirable than pure diamond nanorods, as pure nanorods are, theoretically, excellent thermal conductors and excellent electronic insulators, if the insulating properties are lost, then the product would be less desirable. Further progress was made in 2001 when CVD was used in order to produce diamond-nanorods. However, these nanorods, at 300nm diameter, are relatively large in comparison with the pore size of SBA-15. These nanorods were a breakthrough and even though the dimensions of the nanorods were easily controlled during growth, orientation and ordering of the nanorods was not.[132]

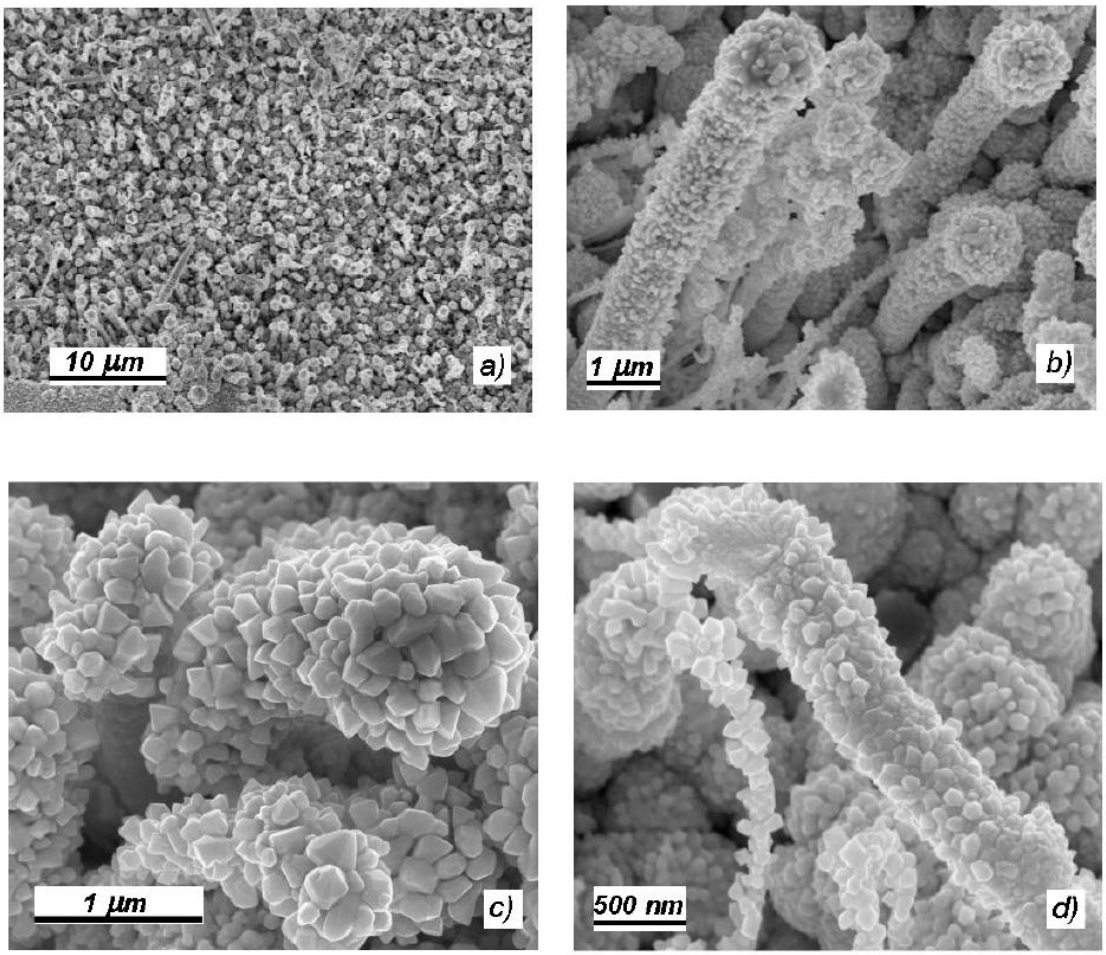

Fig 1.30: (a) The top view of the nanotubes coated with diamond after 15 minutes, The FE-SEM view in (b) complete diamond coverage along the whole length of the tubes. At higher magnifications (c and d) wires are coated by grains with diameters ranging approximately between 20 and 100 nm.[133]

It was not until 2005 that smaller diameter diamond nonowhiskers had been successfully grown by CVD, and even then this process involved a hybrid material, with carbon naontubes, rather than pure diamond nanorods themselves.[133] In this work, Terranova et al, HF-CVD was employed in order to use carbon nanopowders of 40nm mean diameter to grow diamond on the exterior surface. The team behind this work had had previous success in producing carbon nanotubes and used their methods in order to produce the diamond coated carbon nanotubes, shown here in figure 1.30

Microwave plasma CVD has also seen success in creating these hybrid nanotubes, the results of this work produced more success in delivering the much sought after diamond nanorods, shown extending from the supporting carbon nanotube in figure 1.31, however, again, as with the work of Masuda et al, the diamond nanorods were not well ordered.[132, 134]

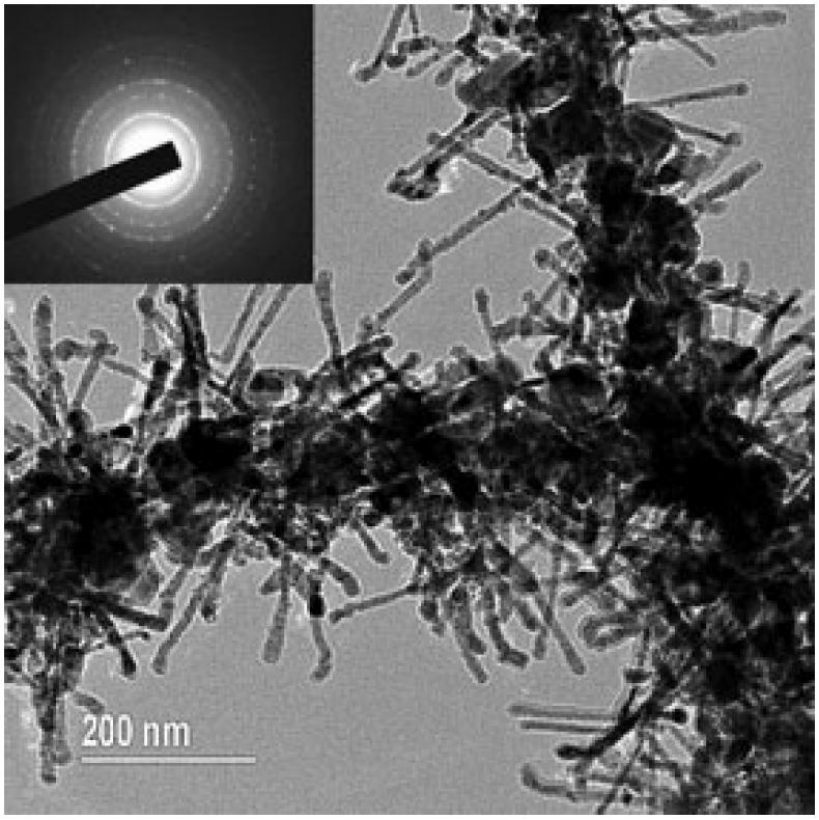

Fig 1.31: TEM image of diamond nanorods grown on the original Carbon nanotube framework.[134]

Nanorods of diamond-fullerene hybrids have also been synthesised.[135] These nanorods have been grown, again by HFCVD. The process requires an ultrananocrystalline diamond substrate doped with 25% N_2. The main difference between these hybrids and the earlier diamond-carbon hybrid nanorods is the fact that, as shown in figure 1.32, the diamond structure is this time on the inside of the fullerene.

(a)

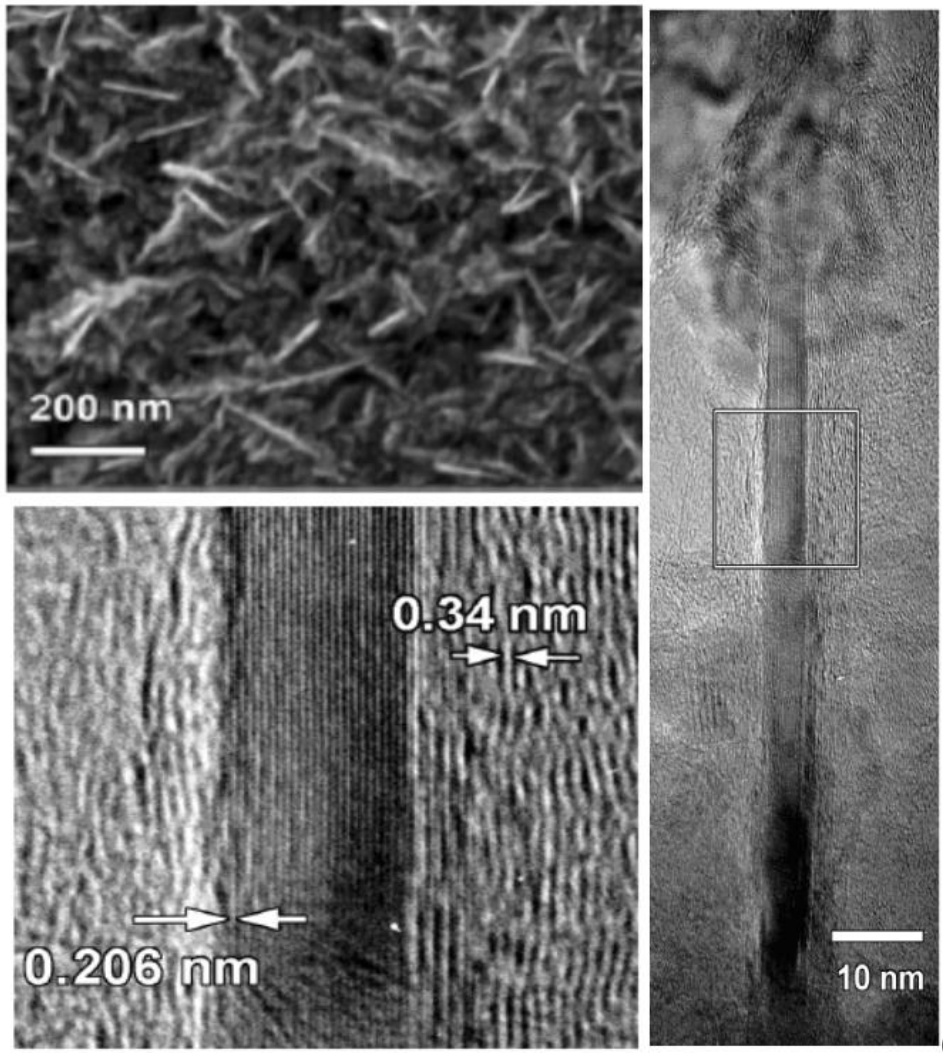

(b) (c)

Fig 1.32: (a) Diamond nanowires protruding from the surface of the 25% N_2 Ultrananocrystalline diamond ssubstrate (b) Close up of Hybrid diamond-fullerene nanorod showing the darker diamond core (c) Hybrid diamond-fullerene nanorod showing the darker diamond core at lower magnification.[135]

Again though with these nanorods, although the fullerene outer layers can theoretically be etched away to leave only the diamond nanorod, the growth of these hybrid nanorods is again disordered, the amount of disorder is shown above in figure 1.32 where the nanorods can clearly be seen overlapping and intersecting.

Reports using ab-initio modelling techniques to obtain theoretical energetic stabilities of diamond nanorods have had favourable results. Initial studies led to the conclusion that the surface morphology of the diamond nanorod and the direction of the internal structure of the diamond nanorod had the largest baring on the stability of the nanorod.[136] Some reported theoretical values hav suggested that at a radius greater than about 1−3 nm, with the correct orientation, a diamond nanorod may have greater physical strength than that of the carbon nanotubes, citing an increase in both the brittle fracture force and zero strain stiffness.[137] This increase in the physical capabilities of diamond nanorods compared with carbon nanorods alone makes them an attractive and viable target for synthesis.[137]

It was with this target that the first diamond nanorods with a radius less than 3nm (6nm diameter) were synthesised. Dubrovinskaia et al, in 2005 reported the first diamond nanorods to be developed with a diameter below 6nm, with a range of 5–20nm.[138] These diamond nanorods were synthesised from fullerene C_{60} in a multi anvil press under 200,000 bar and 2500K. These diamond nanorods were then mechanically tested and proved the modelling theory that the diamond nanorods are the material with the lowest experimentally determined compressibility to date.[138]
The drawbacks to this method are the harsh conditions needed and the energy input required for this high pressure, high temperature synthesis to take place, along with the tendency for non-uniform diamond nanorod formation, rather than the theoretically more energy efficient low pressure low temperature technique of CVD with the use of nanopore templating.

1.6 Aims of This Research

1. Synthesise SBA-15 and CH_3-modified SBA-15 using the cooperative self-assembly method

2. Create nucleation sites within the pores of SBA-15 by incipient wetness impregnation with K_2PtCl_4 solutions and diamond powder suspensions.

3. Investigate the thermal stability of modified SBA-15 for use as a template under HFCVD

4. Produce microcrystalline and nanocrystalline diamond on flat silicon.

5. Optimise parameters for the growth of polycrystalline and nanocrystalline diamond using hot filament CVD and $CH_4/H_2/Ar$ gas mixtures.

6. Undertake the first attempts to use SBA-15 as a template for nanocrystalline diamond rods and by the use of HFCVD deposit diamond within the pores of a sample of SBA-15.

1.7: Experimental Procedures

1.7.1 Mesoporous Silica Oxide Type MCM

1.7.1.1 MCM-41

MCM-41 was synthesized by dissolving Cetyl trimethylammonium bromide (CTAB) (10g) and NaOH (1g) in H_2O (90g) and heated to 35^oC tetraethyl orthosilicate TEOS (11cm^3) was then added and the mixture covered and stirred vigorously. The resulting powder was recovered by filtering and calcined in air by heating to 500 ^oC at 5^oC/min, holding at 500^oC for 6 hours, and then cooling to room temperature over 2 hours.

1.7.1.2 CH_3 Modified MCM-41

Variations of CH_3-MCM-41 were synthesised by following the procedure outlined in 1.7.1.1 with methyltriethyl orthosilicate MTEOS modifier being used in the following proportions alongside the TEOS silicate.

% TEOS	Vol Teos / cm^3	% MTEOS	Vol MTEOS / cm^3
100	11.00	0	0
99	10.89	1	0.09
95	10.45	5	0.50
90	9.90	10	0.90
80	8.80	20	1.80
70	7.70	30	2.71

Table 1.3: The range of concentrations of modifier used in the preparation of CH_3-MCM-41

1.7.2 Mesoporous Silica oxide type SBA-15

SBA-15 was synthesized by dissolving P123 (4g) in distilled water (30g) and HCl (120g), tetraethyl orthosilicate [TEOS] (11cm^3) was added and the solution was stirred for 6 h at 60^oC, followed by 12 hours hydrothermal treatment at 100^oC, the SBA-15 was recovered by filtering and calcined in air by heating to 800^oC at 10^oC/min, holding at 800^oC for 6 hours, and then cooling to room temperature over 4 hours.

1.7.2.1 CH_3 Modified SBA-15

Variations of CH_3-SBA-15 were synthesised by following the procedure outlined in 1.7.2 with methyltriethyl orthosilicate MTEOS modifier being used in the following proportions alongside the TEOS silicate.

% TEOS	Vol Teos / cm^3	% MTEOS	Vol MTEOS / cm^3
100	11.00	0	0
90	9.90	10	0.90
80	8.80	20	1.80
70	7.70	30	2.70
60	6.60	40	3.60
50	5.50	50	4.50
40	4.40	60	5.40
30	3.30	70	6.30

Table 1.4: The range of concentrations of modifier used in the preparation of CH_3-SBA-41

1.7.2.2 Pt Modified SBA-15

Pt-SBA-15 was prepared by an incipient wetness method, impregnating samples of SBA-15 prepared using the method in 1.7.2. Three solutions of K_2PtCl_4 ($1x10^{-4}$ mol dm^{-3}, $1x10^{-3}$ mol dm^{-3} and $1x10^{-2}$ mol dm^{-3}) were prepared and the solutions added dropwise to dry powdered SBA-15 (1g) until the samples showed the first sign of being moist. The samples were then calcined in air by heating to 650 ^{o}C at 25^{o}C/min, holding at 650^{o}C for 6 hours, and then cooling to room temperature over 4 hours.

1.7.2.3 SBA-15 Thermal Stability test.

SBA-15 prepared using the method outlined in 1.7.2 was treated in a calcination oven at 650^{o}C, 750^{o}C, 850^{o}C, 950^{o}C and 1050^{o}C for a period of six hours in air. The sample was then analysed by nitrogen porosimmetry.

1.7.3 Chemical Vapour Deposition (CVD)

The filament was made from 0.5mm diameter tantalum wire and manually formed into a 6 turn coil of diameter 3mm. In this study, a tantalum filament was pre-carbonised for up to 2 hours prior to deposition, using 3 vol % CH_4 in 97 vol % H_2. This is to avoid filament poisoning and tantalum incorporation within the diamond deposit.[139]

Once the substrate has been prepared by abrasion with diamond powder (1-3μm diameter) in order to enhance the nucleation density of diamond on the subtrate, it is fixed to the substrate holder (20mm x 20mm, Mo) using silver glue. Previous research

has established the optimum distance of substrate to filament to be 4 mm for optimum growth of high quality diamond films.[140] The distance of 4mm from the filament to the top of the substrate remained constant throughout deposition experiments.[141] Throughout the deposition procedure the substrate must also be aligned with the filament, as shown in figure 1.33.

Fig 1.33: Photograph of the internal arrangement of the HFCVD reactor. The filament to substrate distance is 4 mm

1.7.3.1 CVD Diamond onto Silicon wafer.

The deposition of diamond onto silicon (Si) wafer was attempted over the gas compositions and pressures listed in Table 1.5. Each setting was run over a period of 3 hours and a period of 6 hours with a flow rate of 20 sccm and a substrate temperature controlled by the filament and kept constant at 850^{o}C measured with a K type thermocouple.

Ar (vol.) %	H_2 (vol.) %	CH_4 (vol.) %	Pressure (Pa)
0	99	1	666.5
0	99	1	2666
0	99	1	6665
0	99	1	13330
25	74	1	666.5
25	74	1	2666
25	74	1	6665
25	74	1	13330
50	49	1	666.5
50	49	1	2666
50	49	1	6665
50	49	1	13330
60	39	1	666.5
60	39	1	2666
60	39	1	6665
60	39	1	13330
80	19	1	666.5
80	19	1	2666
80	19	1	6665
80	19	1	13330
90	9	1	666.5
90	9	1	2666
90	9	1	6665
90	9	1	13330
95	4	1	666.5
95	4	1	2666
95	4	1	6665
95	4	1	13330
99	0	1	666.5
99	0	1	2666
99	0	1	6665
99	0	1	13330

Table 1.5: The gas composition and pressure used in the CVD of diamond onto Silicon wafer.

1.7.3.2 CVD Diamond with SBA-15

Following the CVD experimentation on silicon wafer, the optimum settings for production of the desired nanocrystalline diamond were used to attempt CVD of nanocrystalline diamond within the pores of SBA-15.

The powder was held in a molybdenum tray at a distance of 4mm from the filament and treated for 6 hours at a pressure of 2666 Pa, flow rate of 20 sccm and a gas composition of 95% Ar 4% H_2 1% CH_4 the substrate temperature was controlled by the filament and kept constant at 850^{o}C measured with a K type thermocouple.

1.7.4: Characterisation; SEM, TEM and Porosimmetry.

All SEM images were captured using a Zeiss Supra Model 40VP Scanning Electron Microscope installed at the Dalton Research institute located at Manchester Metropolitan University.

All TEM images were captured using a Philips CM200 FEG microscope located at the Fritz-Haber-Institute, Berlin.

The porosimmetry results were analysed and calculated using a Micromeritics ASAP2020 Surface area Porosity Analyser installed at the Dalton Research institute located at Manchester Metropolitan University.

2

RESULTS AND DISCUSSION

2.1: Results and Discussion

2.1.1 Mesoporous Silica Oxide Type MCM

2.1.1.1 MCM-41

MCM-41 was produced early on in this project as the modification of mesoporous silicates would be more easily tested on a material that took less time to prepare than SBA-15. Figure 2.0 shows the XRD plot from one of the earliest samples of MCM-41 produced, the peaks at 2 theta values of 2.2, 3.4 and 3.8 give three reflections between $2\theta = 2^{o}$ and $2\theta = 5^{o}$, just as in figure 1.7 (a). The small peak at $2\theta = 6.9$ indicates that there is a small amount of MCM-50 stable within the structure also. The production of MCM-41 following the procedure outlined in section 1.7.1.1 was easily reproducible and therefore it was relatively easy to design the method for the modification of MCM-41 with CH_3 groups.

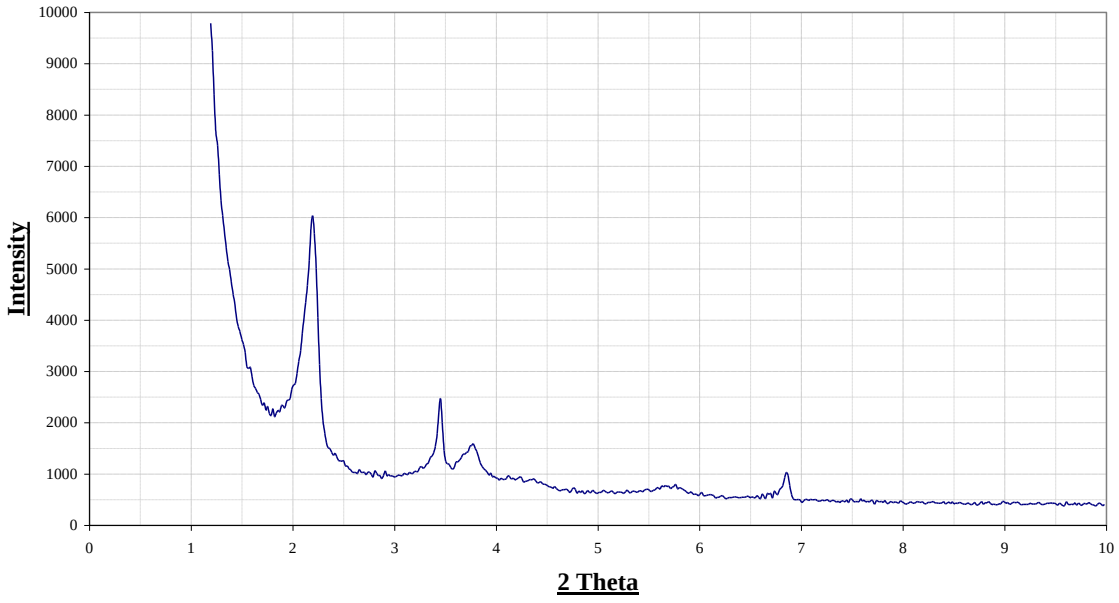

Fig 2.0: XRD plot of MCM-41 prior to calcination

2.1.1.2 CH_3 Modified MCM-41

The MCM derivatives produced following the method in section 1.7.1.2 shown in figure 2.1 have mesopore stability when produced using up to 30% MTEOS modifier. Up to the 30% MTEOS modification, the XRD show pore structures with three reflections in the 2θ =2-5 range. As the amount of modifier, the number and quality of these peaks decreases.

Replacing 30% of the TEOS with MTEOS allows for a significant number of organic groups present within the structure of MCM-41 like materials. This posed the question as to whether the same could be accomplished with SBA-15, a more useful substrate due to the pore size of SBA-15.

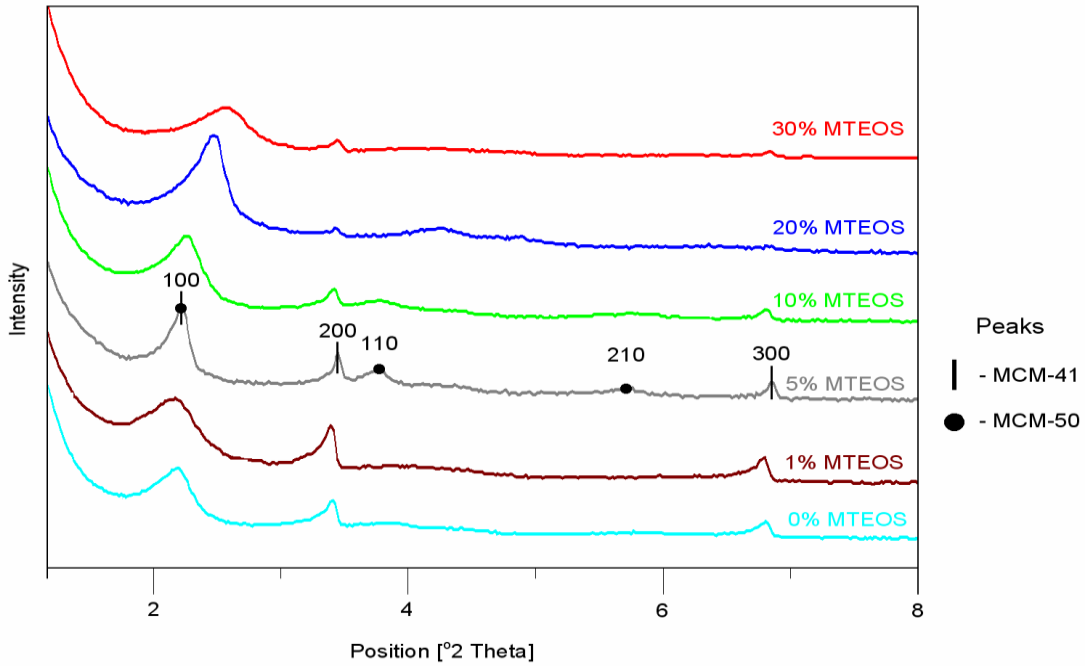

Fig 2.1: XRD plot of MCM derivatives with a range of CH_3 modifier.

2.1.2 Mesoporous Silica oxide type SBA-15

The SBA-15 produced experimentally using the method outlined in section 1.7.2 is stable in air up to a temperature of 750^{o}C, as is shown by the thermal stability testing discussed in 2.1.2.3. There are good areas of pore structure present as shown in the XRD plot (see figure 2.2) and the TEM images of the SBA samples shown in figure 2.3, with the (100) reflection at 2θ = 0.8, the (110) reflection at 2θ = 1.5 and the (200) reflection 2θ = 1.7, as shown in figure 1.8. This success in synthesising SBA-15 was the successful stepping stone required to be able to produce modified versions of SBA-15 for use in the synthesis of diamond nano-wires.

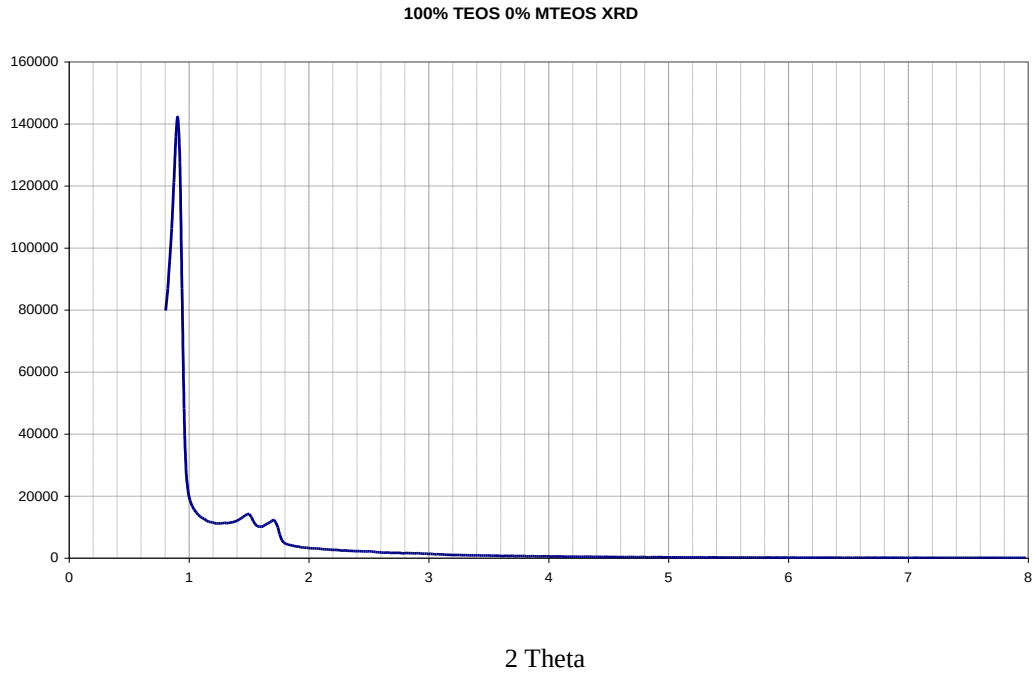

Fig 2.2: XRD plot of SBA-15

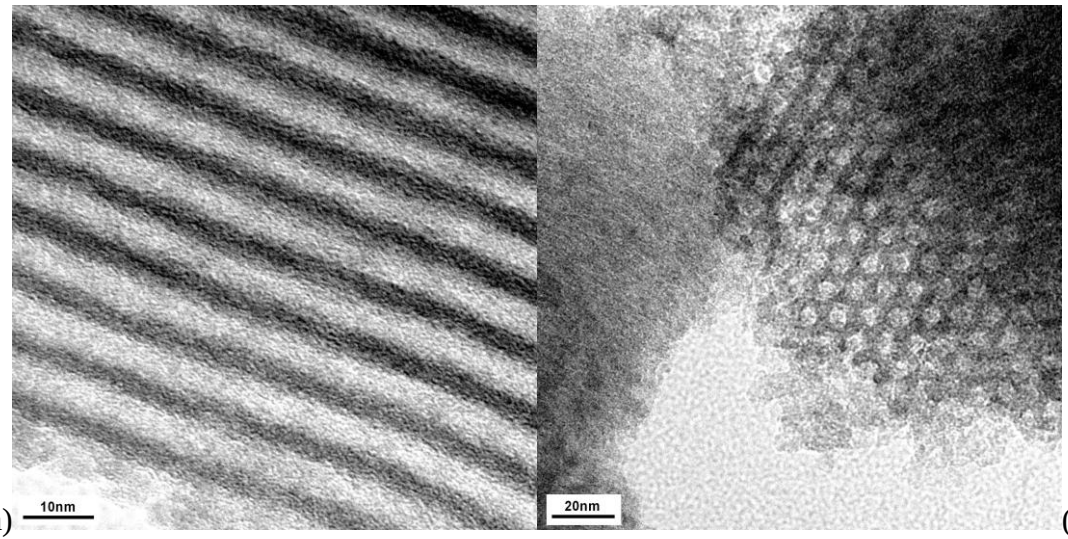

(a) (b)

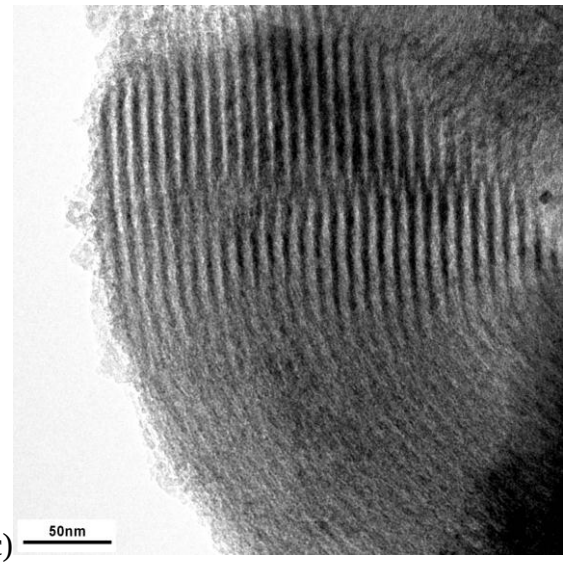

(c)

Fig 2.3: TEM images of SBA-15 recorded on a Philips CM200 FEG microscope, operated at an accelerating voltage of 200kV. (a) Regular pore structure is shown with a diameter of 5nm. (b) Hexagonal arrangement of the cylindrical pores of SBA-15 (c) Pores of Sba-15 clearly shown over a large area relative to the sample size.

2.1.2.1 CH_3 Modified SBA-15

The attempt to modify SBA-15 was taken in order to provide a surface that would be more likely to induce nucleation of diamond under CVD. The CH_3 modified SBA-15, synthesised by the method in section 1.7.2.1, was found to have some pore stability up

to a maximum of 40% modifier, however, the highest percentage of MTEOS modifier used that was regularly seen to produce a stable product was 30%. Figure 2.4 below shows the degradation of pore stability as the percentage of the modifier is increased. We see this as when the amount of modifier increases, there is a shift in the pattern and intensity of the XRD. As the amount of modifier increases the intensity of the peaks decrease pore structure of MCM-41 being completely lost at the point where 70% of the reacting silicate is MTEOS.

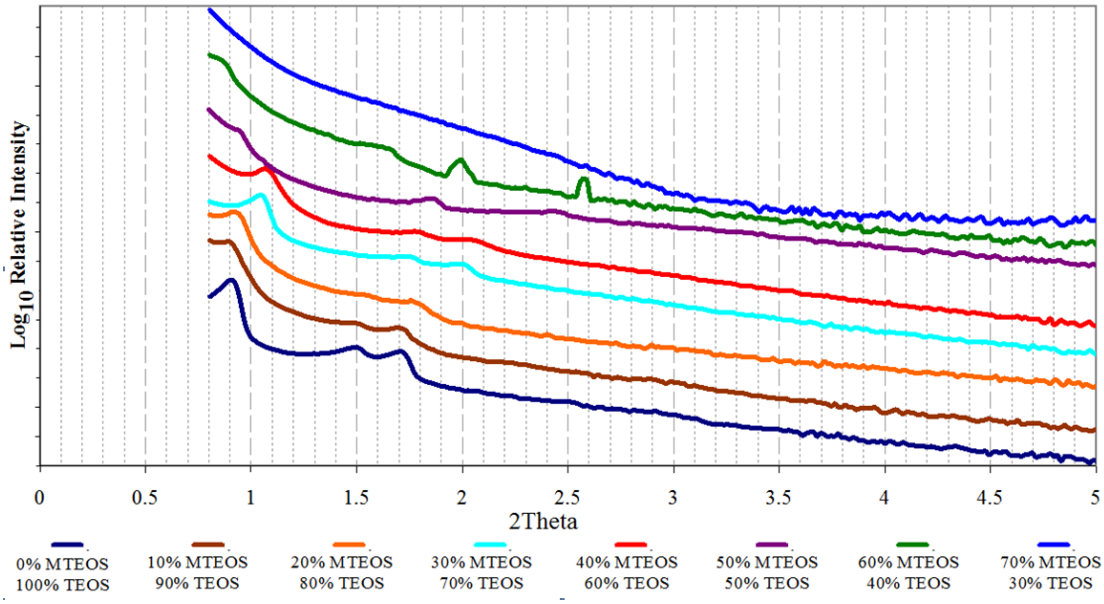

Fig 2.4: Log_{10} XRD plot of CH_3-SBA-15 showing the ratio of TEOS to MTEOS used, where the MTEOS is providing the CH_3 modification to SBA-15, and its effect on pore structure.

A stable SBA-15 structure with 30% MTEOS modifier still provides the possibility of many CH_3 groups lining the inside of the SBA-15 pores as possible nucleation sites for CVD. However it is not certain at this point that the structure of the CH_3-SBA-15 would have the CH_3 groups on the surface of the pore or whether the CH_3 groups would be within the structure.

Nitrogen porosimmetry was performed on the samples in order to establish where the CH_3 groups were located within the structure. In figure 2.5 we see an increase in pore diameter as the amount of modifier increases. This is an indication that the CH_3 may be within the pores of the SBA-15 structure. Based upon this, the CH_3-SBA-15 samples seem to be viable for testing as possible substrates for enhanced nucleation for CVD of nanocrystalline diamond within a porous structure.

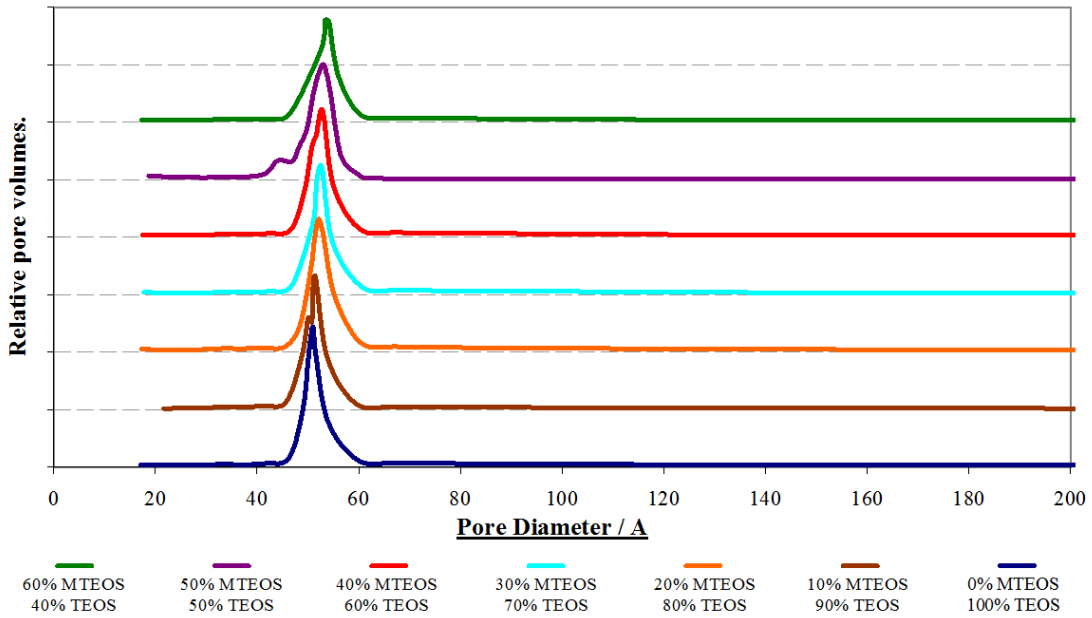

Fig 2.5: Nitrogen porosimmetry of CH_3-SBA-15 showing the ratio of TEOS to MTEOS used, where the MTEOS is providing the CH_3 modification to SBA-15, and its effect on pore size.

% MTEOS/%TEOS	60/40	50/50	40/60	30/70	20/80	10/90	0/100
Pore Diameter / Å	54.1	53.1	52.9	52.7	52.1	51.4	51.0

Table 2.1: Nitrogen porosimmetry data for CH_3-SBA-15 showing the ratio of TEOS to MTEOS used, where the MTEOS is providing the CH_3 modification to SBA-15, and its effect on pore diameter.

2.1.2.2 Pt Modified SBA-15

The first test in producing the platinum doped SBA-15 was to observe the method for stability. The original SBA-15 was treated only with de-ionised water and then dried. In this experiment the SBA-15 was treated with the K_2PtCl_4 solution and then dried. The outcome, shown in figure 2.6 indicates that the pore is unchanged under the treatment method and that there is a 30% decrease in the pore volume when doped with platinum.

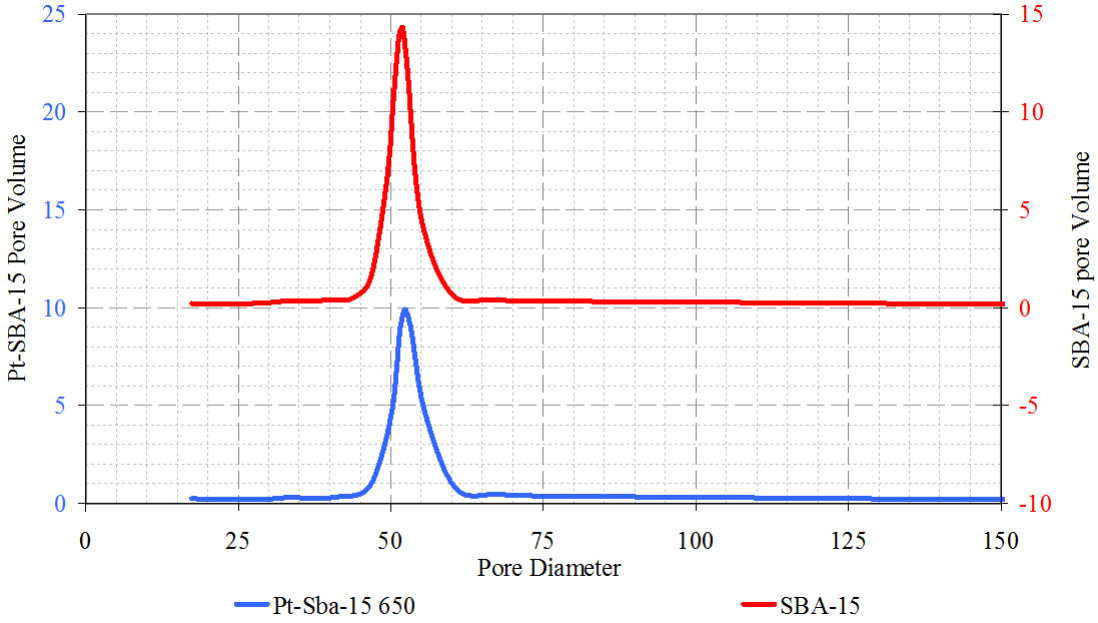

Fig 2.6: Nitrogen porosimmetry plot of Pt-SBA-15.

When the samples of Pt impregnated SBA-15 were examined by nitrogen porosimmetry, they were found to have a lower pore volume when the concentration of the Pt complex was increased. This was in line with the hypothesis that a greater initial complex concentration would lead to a greater nucleation of Pt within the pores. Figures 2.7 and 2.8 show how the pore size changes, the pore structure has not

changed significantly. There is a slight decrease in pore volume, which increases as the K_2PtCl_4 concentration increases. This suggests that the pores have been partially filled with platinum nucleation sites for CVD. This is also indicated in fig 2.9, where the pore volume increases as the amount of K_2PtCl_4 modifier decreases, indicating that there is a deposit of something else within the pores.

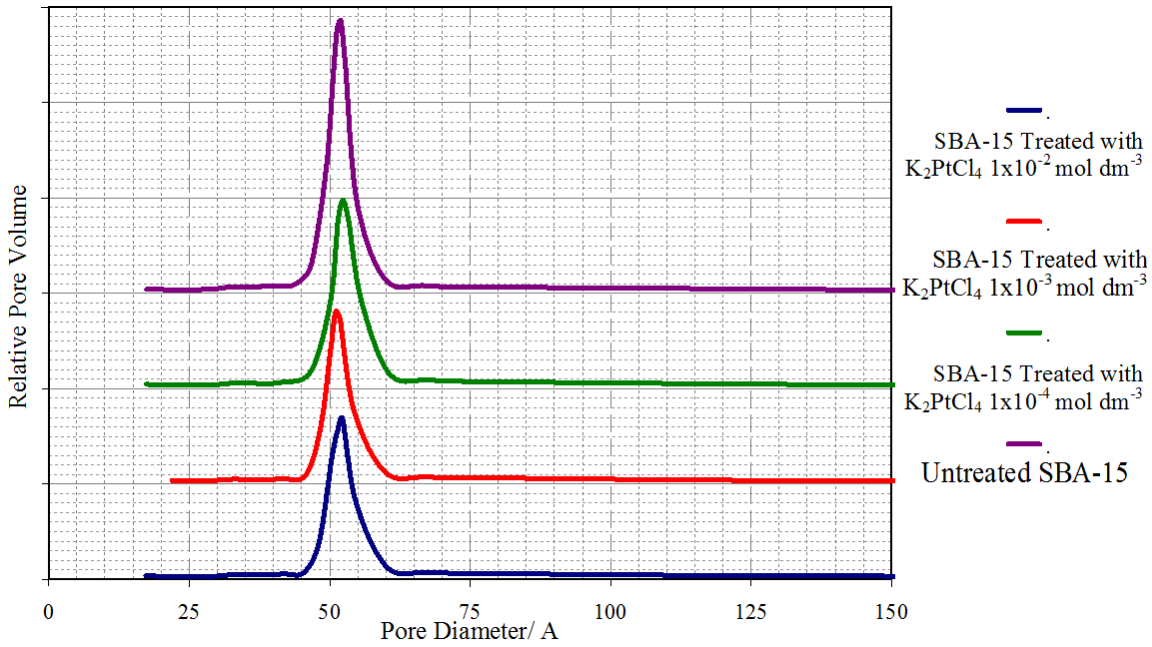

Fig 2.7: Nitrogen porosimmetry plot of Pt-SBA-15 prepared by incipient wetness using K_2PtCl_4 ($1x10^{-2}$mol dm^{-3}-$1x10^{-4}$mol dm^{-3}) including the result when SBA-15 was treated in the same way with de-ionised water.

SBA-15 treated with K_2PtCl_4	$1x10^{-2}$ mol dm^{-3}	$1x10^{-3}$ mol dm^{-3}	$1x10^{-4}$ mol dm^{-3}	Untreated
Pore Diameter / Å	52.3	51.9	52.3	52.0
Pore Volume cm^3/g	8.4	13.6	19.9	29.3

Table 2.2: Nitrogen porosimmetry data for Pt-SBA-15 prepared by incipient wetness using K_2PtCl_4 ($1x10^{-2}$mol dm^{-3}-$1x10^{-4}$mol dm^{-3}) including the result when SBA-15 was treated in the same way with de-ionised water.

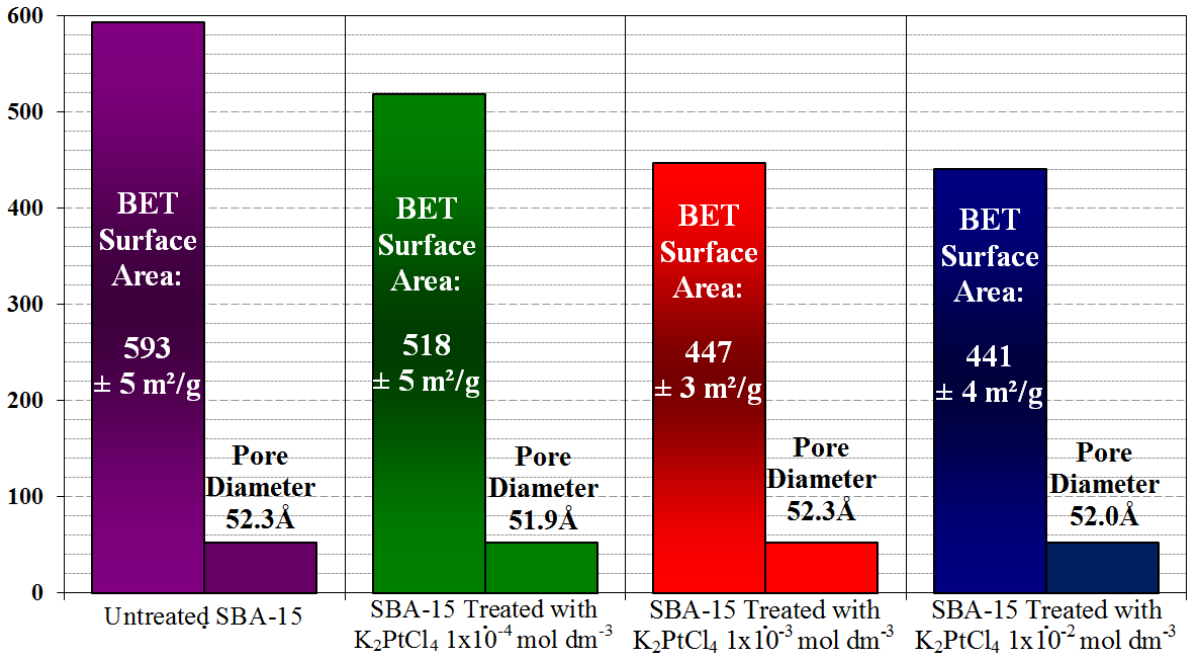

Fig 2.8: BET surface area values and pore diameters for Pt-SBA-15 prepared by incipient wetness using K_2PtCl_4 ($1x10^{-2}$mol dm^{-3}-$1x10^{-4}$mol dm^{-3}) including the result when SBA-15 was treated in the same way with de-ionised water.

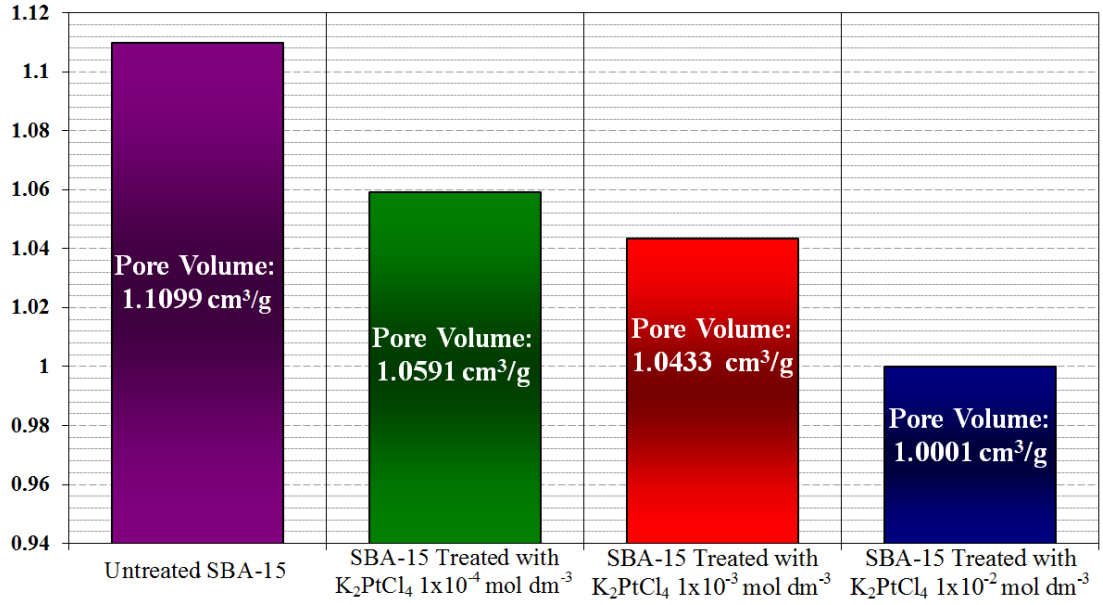

Fig 2.9: Pore Volumes for Pt-SBA-15 prepared by incipient wetness using K_2PtCl_4 ($1x10^{-2}$mol dm^{-3}-$1x10^{-4}$mol dm^{-3}) including the result when SBA-15 was treated in the same way with de-ionised water.

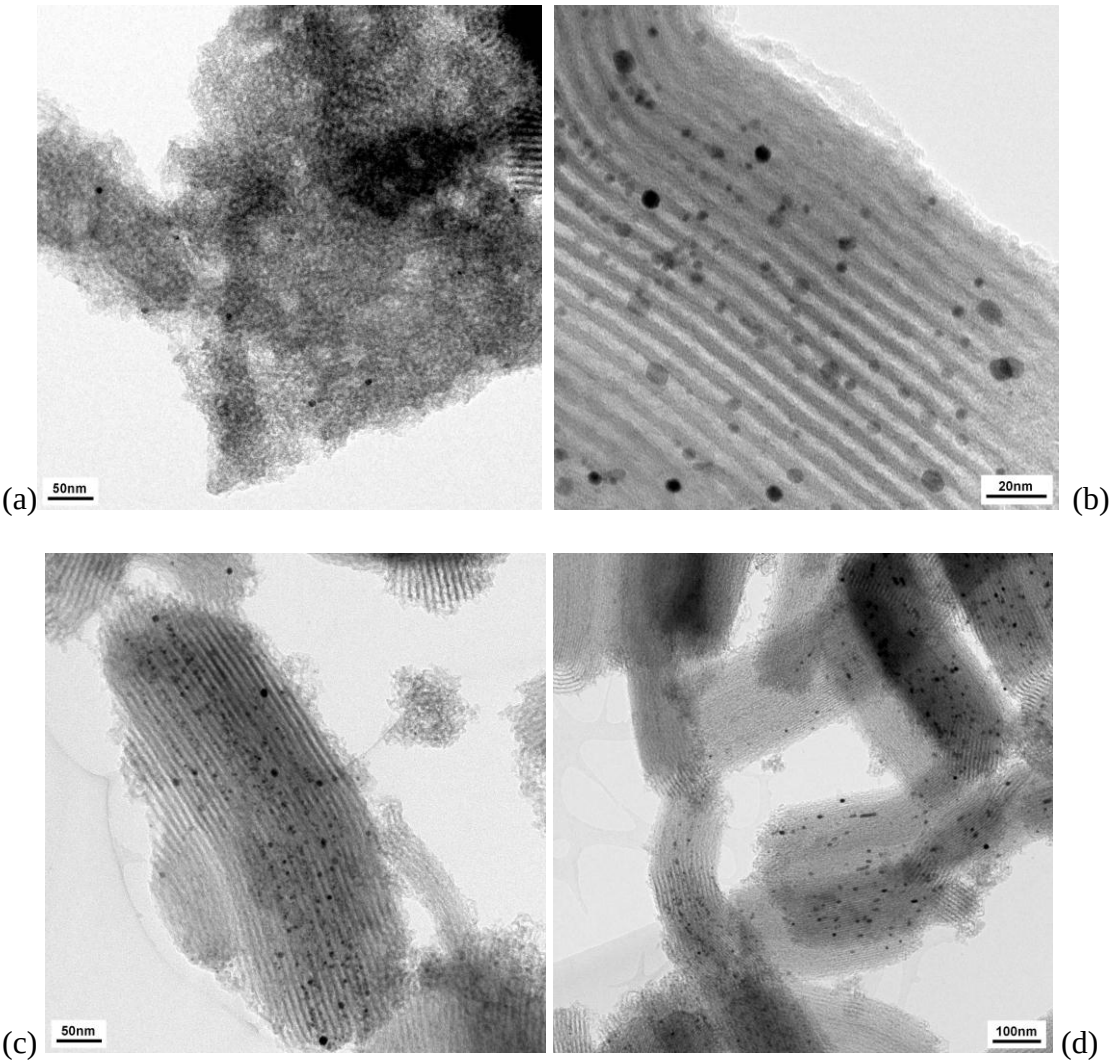

Fig 2.10: TEM image of Pt-SBA-15 prepared by the incipient wetness method laid out in section 1.7.2.2 using K_2PtCl_4 $1x10^{-2}$ mol dm^{-3} (a) amorphous silica oxide with 4 clear Pt nucleations, (b) ordered silica oxide with clear Pt nucleations within the pores of SBA-15, (c) Clear area of dense nucleation of Pt, (d) a larger image showing a constant impregnation of Pt nucleation within the pore structure of the SBA-15. The images were recorded on a Philips CM200 FEG microscope, operated at an accelerating voltage of 200kV

From the TEM images in fig 2.10, (a) suggests some of the structure of SBA-15 has either not formed, or has collapsed under the treatment, however, this area was found to be small in comparison with the area of SBA-15 sample with good structure. Included in this is the observation that there are relatively few areas of platinum

nucleation in this area. There is a greater nucleation of platinum shown in the structured areas of SBA 15, (b-d) showing the platinum embedded within the pores of the SBA-15 structure.

2.1.2.3 SBA-15 Thermal Stability test.

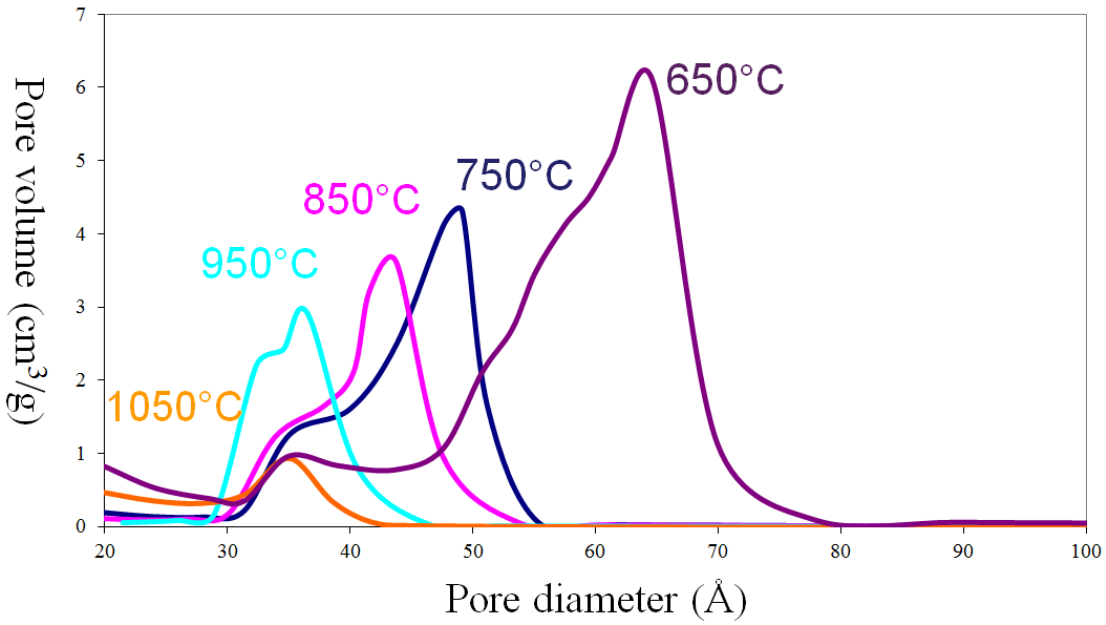

Fig. 2.11: Pore size distribution plots of SBA-15 after elevated temperature treatment for 6 hours in air.

The pore size distribution plots for SBA-15 treated at temperatures between 650 °C and 1050 °C in air for 6 hours are show in figure 2.11. There is some damage to pore structure even at 750 °C, shown by a decrease in pore diameter. This may indicate that SBA-15 is not sufficiently thermally stable to withstand the conditions of diamond CVD, however, there is still SBA-15 like porous structure even after treatment in air at 850°C, meaning that the deposition of diamond nano-wires may be equally plausible. Significantly the structure remains porous even after treatment at high temperatures, meaning that there may be useful pores for diamond nanowire growth even at these higher temperatures.

2.1.3 Chemical Vapour Deposition (CVD)

2.1.3.1 CVD Diamond onto Silicon wafer.

What appeared under SEM to be microcrystalline diamond shown in Fig 2.12 and 2.13 was produced using a run time of 6 hours at a pressure of 2666 Pa, flow rate of 20 sccm and a gas composition of 99% H_2 1% CH_4. The silicon wafer substrate temperature was controlled by the filament and kept constant at 850^{o}C. This was consistent and repeatable and formed of relatively large crystals of diamond upon silicon wafer. However, the discontinuous surface coverage of the diamond indicates that there is a relatively poor density of nucleation sites.

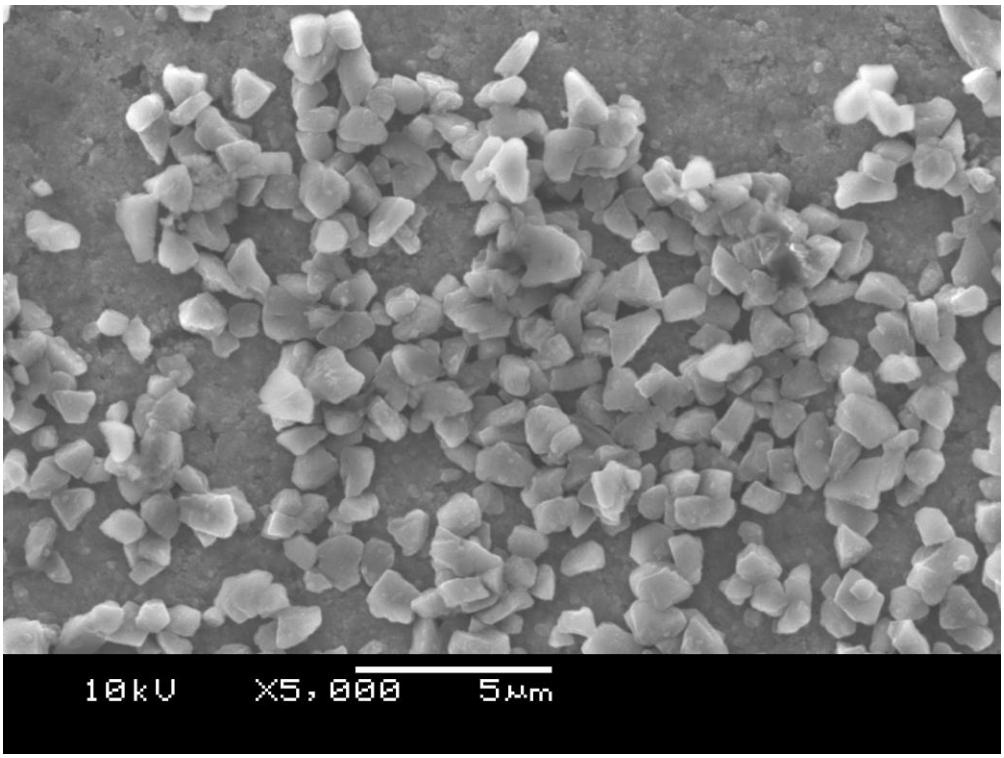

Fig 2.12: SEM image of microcrystalline diamond grown on silicon wafer.

Recorded on a Zeiss Supra Model 40VP SEM

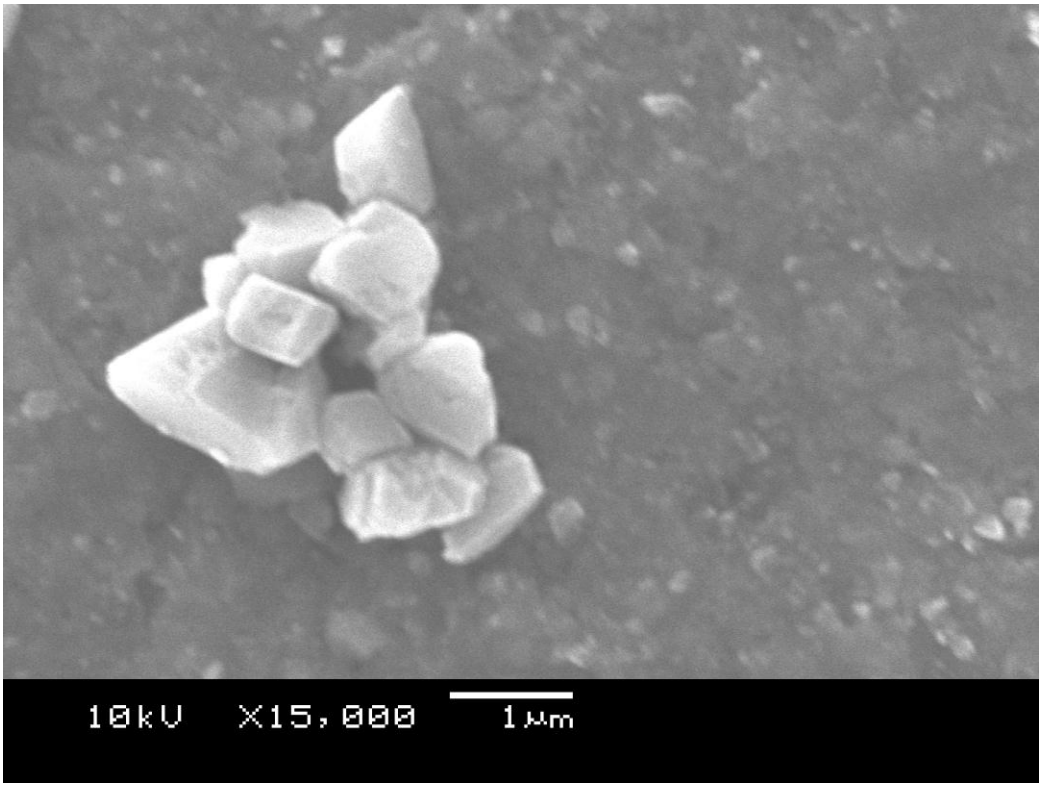

Fig 2.13: SEM image of a second sample of microcrystalline diamond grown on silicon wafer this time shown at a higher magnification. Recorded on a Zeiss Supra Model 40VP SEM

What appears to be nanocrystalline diamond was produced using the same run time, temperature and pressure, but using a change in the gas composition of 95% Ar 4% H_2 1% CH_4. This resulted in a change in the nature of the diamond deposited; the deposition of one sample is shown in fig 2.14 and 2.15. The surface coverage of the nanocrystalline diamond is more complete than that of the microcrystalline diamond, This is evident on comparing figure 2.12 and 2.14, where the surface has almost complete coverage of nanocrystalline diamond, whereas the microcrystalline diamond previously deposited has silicon wafer remaining exposed. The size and structural comparison between the two samples is shown upon comparing figure 2.13 and 2.15,

where the diameter of the diamond crystal deposited on the silicon wafer in figure 2.13, at its smallest, ~0.9µm compared with the sample shown in figure 2.14 where the individual crystals are still too small to be measured with any reliable degree of accuracy using SEM techniques.

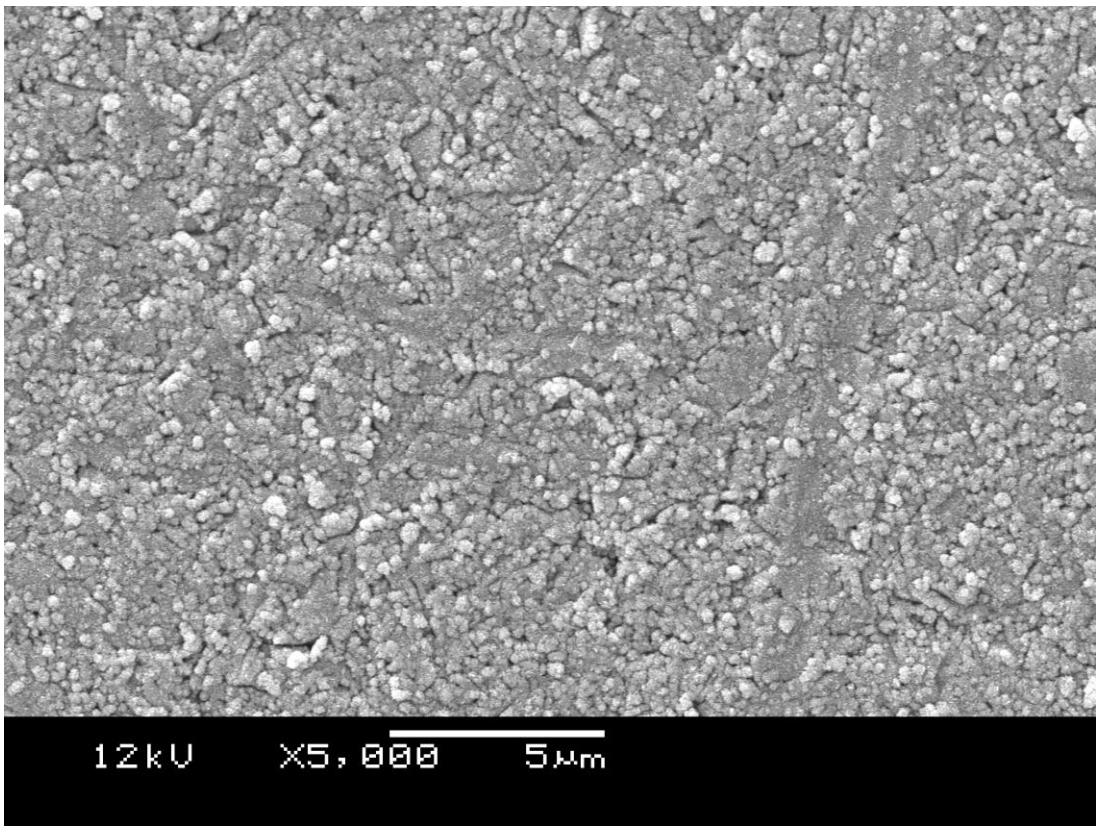

Fig 2.14: SEM image of nanocrystalline diamond grown on silicon (Si) wafer. Recorded on a Zeiss Supra Model 40VP SEM

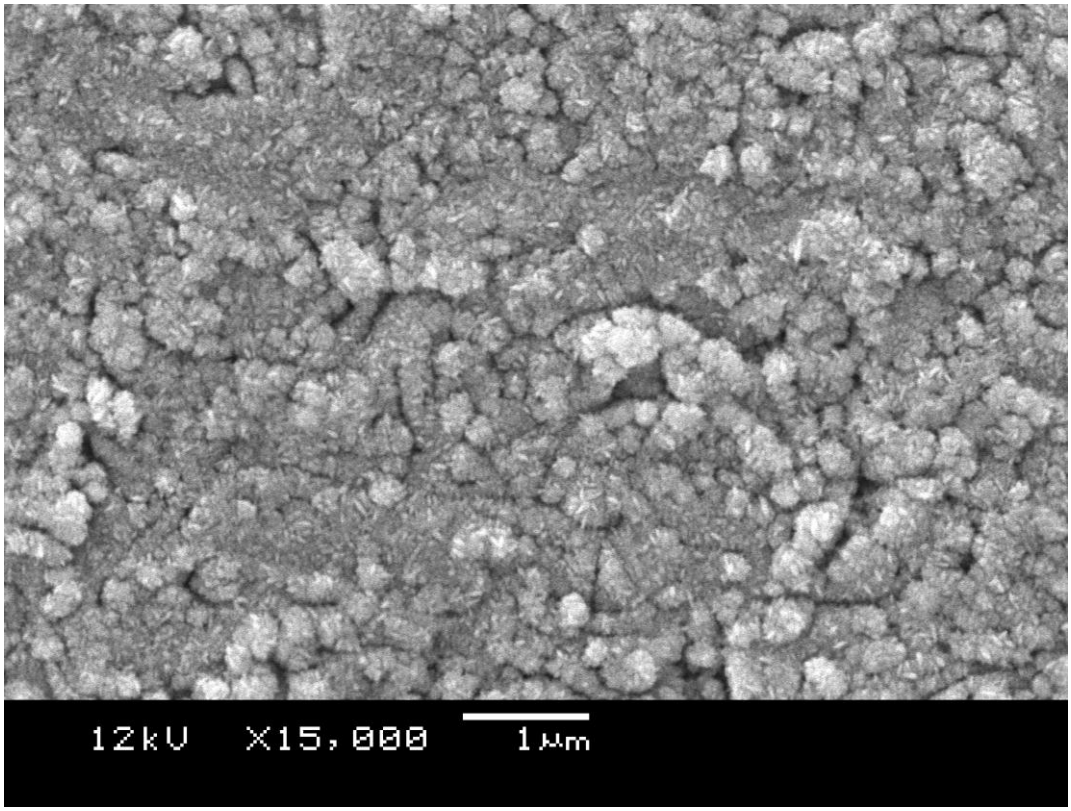

Fig 2.15: SEM image of the nanocrystalline diamond grown on silicon (Si) wafer from fig 2.12 shown in higher magnification. Recorded on a Zeiss Supra Model 40VP SEM

In this section it is important to note that even though the appearance of the diamond grown on the silicon wafer is that of micro and nanocrystalline diamond, there is no complete set of results here that prove conclusively that this is either of the diamond types. In order for this to be known fully Raman spectroscopy of the samples would be required.

The size of the microcrystalline diamond grown (~10,000Å) was deemed unsuitable for deposition onto SBA-15 and its derivatives as the size of the crystals were too

large for the pores (~52Å). It was therefore decided that the conditions for nanocrystalline diamond growth should be used with SBA-15.

2.1.3.2 CVD Diamond with SBA-15

Initially it was decided to test the stability of SBA-15 under deposition conditions by attempting nanocrystalline diamond deposition on untreated SBA-15. The sample of SBA-15 that was placed into the CVD rig, shown in figure 2.16 was very different from the sample after CVD using conditions for the growth of nanocrystalline diamond. There were two distinct layers, an upper layer, (figure 2.17) which was black in appearance and a lower layer (figure 2.18) which appeared unchanged by the CVD process. The layers were examined both individually and together by mass comparison, nitrogen porosimmetry and XRD. The difference in the visual characteristics could have been caused by diamond deposition within the pores of the upper layer of the SBA-15.

Fig 2.16: Photograph of SBA-15 prior to CVD

Fig 2.17: Photograph of SBA-15 top layer after CVD

Fig 2.18: Photograph of SBA-15 lower layer after CVD

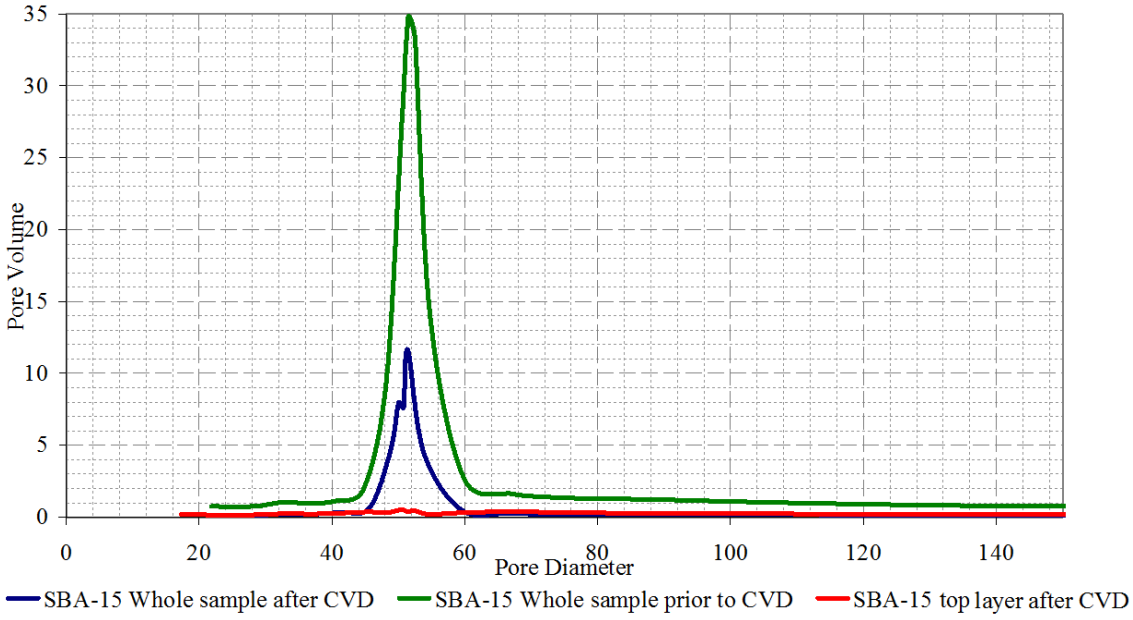

Fig 2.19: Nitrogen porosimmetry of SBA-15 before and after CVD with a substrate temperature of 850^{o}C using whole sample.

The nitrogen porosimmetry data (figure 2.19) was inconclusive. When the whole sample was compared with an SBA-15 sample prior to CVD, the results seem to suggest that there may be pore filling. When the comparison was made with the top layer, the same conclusion could be reached, it seems as though the layer closest to the filament has had carbon deposited in the pores, whilst deeper into the material there is little to no deposition taking place.

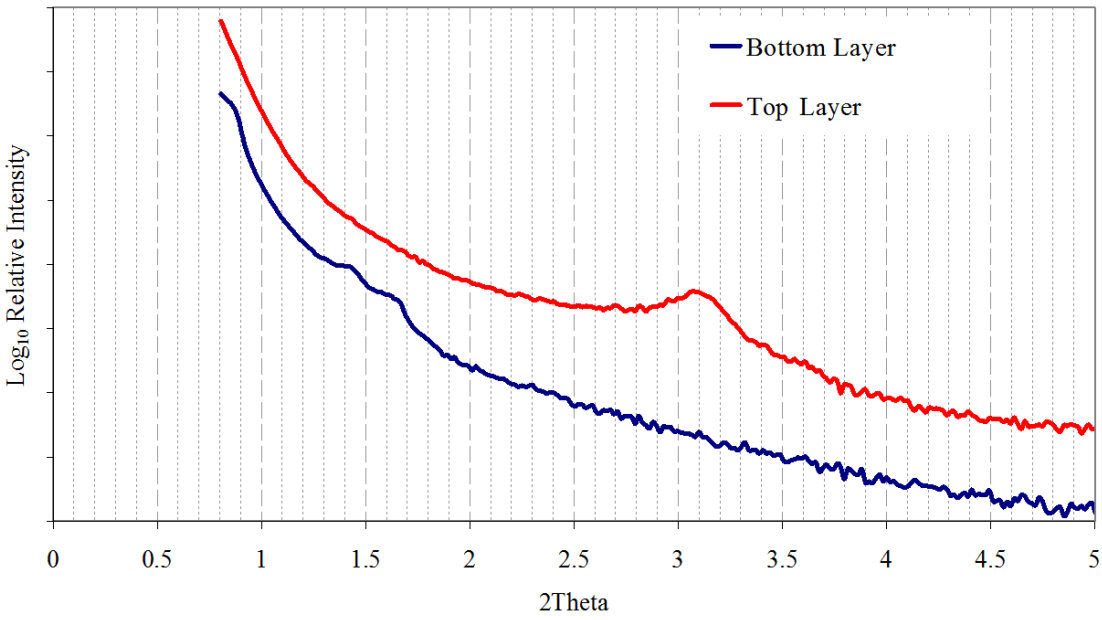

Fig 2.20: XRD plot of SBA-15 layers.

The XRD spectra, shown here in figure 2.20 as a $\log_{10}$ plot, presents evidence that the SBA-15 sample is degrading in the CVD chamber during the carbon deposition into the top layer. Figure 2.20 shows the top layer as having no ordered SBA-15 structure remaining, there is possibly some form of order within the powder, shown by the peak at the 2 theta value 3.1, however, this does not resemble the order for that of SBA-15 as sought. The lower layer of powder still has a weak XRD spectrum resembling that of SBA-15. This result could also explain why there is some porous characteristic

remaining when examining the nitrogen porosimmetry in fig 2.19. The lowered pore volume is most likely due to deposition of carbon in the top layer of the SBA-15 sample whilst the remaining pore volume can be explained by the fact that the lower half of the treated SBA-15 held some of its structure.

3

CONCLUSIONS

3: Conclusions

1. SBA-15 materials with pore diameters between 5 and 6 nm, with narrow pore size distribution and surface areas ~500 m^2 g^{-1}have been successfully synthesised.

2. There were obvious platinum nucleation sites within the pores of SBA-15 formed by incipient wetness impregnation with K_2PtCl_4 solutions.

3. SBA-15 has been shown to retain some pore structure at temperatures used in nanodiamond CVD.

4. On silicon wafers there have been successful depositions of, what appears under SEM, to be microcrystalline and nanocrystalline diamond.

5. The optimum conditions for the apparent nanocrystalline diamond growth have been found to be: gas composition 95% Ar, 4% H_2, 1% CH_4 at a flow rate of 200 SCCM and substrate temperature 950 °C.

6. SBA-15 samples have been introduced to the CVD chamber as a substrate for deposition. Despite early results showing less promise than was hoped, there is still reason to believe that the technique can produce nanowires within the pores of SBA-15. Future Raman spectroscopy and TEM work would be required to discover more about the top layer of the material produced after CVD of the SBA-15 samples.

4

RECOMMENDATIONS FOR FUTURE WORK

4: Recommendations for Future Work.

1. Transmission Electron Mictoscopy (TEM) Should be carried out on all SBA-15 samples produced by CVD, to investigate (a) what has happened to the structure of the pores and (b) whether there has been any deposition of a substance within the pores.

2. Raman Spectroscopy should be carried out on all samples that have undergone CVD to establish the nature of the diamond deposited.

3. Further CVD should be carried out on mesoporous silica oxides in order to determine if there is a point at which the substrate is stable under deposition conditions.

4. Work can be continued on creation of mesoporous oxides that are both stable at deposition temperatures already known to be successful and have a pore size of 50Å, matching the pore size that has been worked out theoretically as preferential for diamond deposition within pores.

5

REFERENCES

5: References

1.) J. Arika, K. I. Shinnanyo, Y. T. Tokuyama, 1985, US Patent No. 4530824.

2.) J.D. Sherman, Synthetic Zeolites and Other Microporous Oxide Molecular Sieves. *Proc. Natl. Acad. Sci. USA*, 1999, Vol. 96, **3471–3478**

3.) R.G. Bell, *What Are Zeolites?*[online]. Published online: British Zeolite Association. Available at: http://www.bza.org/zeolites.html, 2001, [Accessed: December 2011]

4.) K. Hermann, *Gallery of BALSAC (and other) pictures* [Online]. Published online: Fritz Haber Institute of the Max Planck Society. Available at: http://www.fhi-berlin.mpg.de/~hermann/Balsac/BalsacPictures/Sodalite.gif, 2011, [Accessed: December 2011]

5.) US Department of the Interior: Bureau of Mines, Natural and Synthetic Zeolites. *Information Circular*, 1987, Vol. 9140, **3**

6.) W. Locke, *Structure*[Online]. Published Online: Imperial College London. Available at: http://www.ch.ic.ac.uk/vchemlib/course/zeolite/structure.html, 1997, [Accessed: December 2011]

7.) W.Lowenstein, The Distribution of Aluminum in the Tetrahedra of Silicates and Aluminates, *American Mineralogist*, 1954, Vol. 39, **92**

8.) M.E. Landis, B.A. Aufdembrinck, P. Chu, I.D. Johnson, G.W. Kirker, M.K. Rubin, Preparation of Molecular Sieves from Dense Layered Metal Oxides. *J. Am. Chem. Soc.*, 1991, Vol.113, **3189**

9.) C. T. Kresge, M. E. Leonowicz, W. J. Roth, J. C. Vartuli, J. S. Beck, Ordered Mesoporous Molecular Sieves Synthesized by a Liquid-Crystal Template Mechanism, *Nature*, 1992, Vol. 359**, 710**

10) J. S. Beck, J. C. Vartuli, W. J. Roth, M. E. Leonowicz, C. T. Kresge, K. D. Schmitt, C. T-W. Chu, D. H. Olson, E. W. Sheppard, S. B. McCullen, J. B. Higgins, J. L. Schlenker, A New Family of Mesoporous Molecular Sieves Prepared With Liquid Crystal Templates, *J. Am. Chem. Soc.*, 1992, Vol. 114, **10834**

11.) V. Chiola, J. E. Ritsko, C. D. Vanderpool, 1971, US Patent No. 3556725.

12.) F. DiRenzo, H. Cambon, R. Dutartre, A 28-Year-Old Synthesis of Micelle-Templated Mesoporous Silica, *Microporous Mater.*, 1997, Vol. 10, **283**

13.) J. S. Beck, 1991, US Patent No. 5057296.

14.) D. Zhao, J. Feng, Q. Huo, N. Melosh, G.H. Fredrickson, B.F. Chmelke, G.D. Stucky, Triblock Copolymer Syntheses of Mesoporous Silica with Period 50 to 300 Angstrom Pores. *Science*. 1998, Vol 279, issue 5350, **548-552**

15.) M.E. Davies, Large and extra-large pore molecular sieves, *Chemistry and Industry*, 1992, Vol. 4, **137**

16.) H.H.P. Yiu, C.H. Botting, N.P. Botting and P.A. Wright, Size selective protein adsorption on thiol-functionalised SBA-15 mesoporous molecular sieve, *Phys. Chem. Chem. Phys.*, 2001, Vol. 3, **2983-2985**

17.) S. Perathoner, P. Lanzafame, R. Passalacqua, G. Centi, R. Schlögl, D.S. Su, Use of mesoporous SBA-15 for nanostructuring titania for photocatalytic applications**,** *Microporous and Mesoporous Materials*, 2006, Vol.90, **347-361**

18.) H. Yang, D. Zhao, Synthesis of replica mesostructures by the nanocasting strategy, *J. Mater. Chem*. 2005, Vol. 15, **1217–1231**

19.) S. Jun, S.H. Joo, R. Ryoo, M. Kruk, M. Jaroniec, Z. Liu, T. Ohsuna, O. Terasaki, Synthesis of New Nanoporous Carbon with Hexagonally Ordered Mesostructure, *J. Am. Chem. Soc.* 2000, Vol 122, **10712-10713**

20.) J. S. Beck, J. C. Vartuli, G. J. Kennedy, W. J. Roth, S. E. Schramm, Molecular or Supramolecular Templating: Defining the Role of Surfactant Chemistry in the Formation of Microporous and Mesoporous Molecular Sieves, *Chem. Mater*., 1994, Vol. 6, **1816**

21.) A.M. Doyle, B.K. Hodnett, Synthesis of 2-Cyanoethyl Modified MCM-48 Stable to Surfactant Removal by Solvent Extraction: Influence of Organic Modifier, Base and Surfactant, *Microporous Mesoporous Mater*., 2003, Vol. 58, **255**

22.) A. Firouzi, D. Kumar, L.M. Bull, T. Besier, P. Sieger, Q. Huo, S.A. Walker, J.A. Zasadzinski, C. Glinka, J. Nicol, Cooperative organization of inorganic-surfactant and biomimetic assemblies, *Science*, 1995, Vol. 267, Issue 5201, **1138-1143**

23.) Z.Jin, X. Wang, X. Cui, Synthesis and morphological investigation of ordered SBA-15-type mesoporous silica with amphiphilic triblock copolymer template under various conditions, *Colloids and Surfaces A: Physicochem. Eng. Aspects*, 2008, Vol. 316, **27-36**

24.) D. Zhao, J. Sun, Q. Li, G.D. Stucky, Morphological Control of Highly Ordered Mesoporous Silica SBA-15, *Chem. Mater*., 2000, Vol. 12 (2), **275–279**

25.) S. Ruthstein, V. Frydman, S. Kababya, M. Landau, D. Goldfarb, Study of the Formation of the Mesoporous aterial SBA-15 byEPR Spectroscopy, *J. Phys. Chem.B.*, 2003, Vol 107, **1739-1748**

26.) D. Zhao, Q. Huo, J. Feng, B.F. Chmelka, G.D. Stucky, Nonionic Triblock and Star DiblockCopolymer and Oligomeric Surfactant Syntheses of Highly Ordered, Hydrothermally Stable, Mesoporous Silica Structures. *J. Am. Chem. Soc.* 1998, Vol. 120, **6024-6036**

27.) S. Ruthstein, J. Schmidt, E. Kesselman, Y. Talmon, D. Goldfarb, Resolving Intermediate Solution Structures during the Formation of Mesoporous SBA-15, *J. Am. Chem. Soc.* 2006, Vol. 128 (10), **3366-3374**

28.) U. Ciesla, D. Demuth, R. Leon, P. Petroff, G. D. Stucky, K. Unger, F. Schuth, Surfactant Controlled Preparation of Mesostructured Transition-metal Oxide Compounds, *J. Chem. Soc. Chem. Comm.*, 1994, Vol. 11, **1387**

29.) Q. Huo, D. Margolese, U. Ciesla, P. Feng, T. E. Gier, P. Sieger, R. Leon, P. Petroff, F. Schuth, G. D. Stucky, Generalized Synthesis of Periodic Surfactant/Inorganic Composite Materials. *Nature*, 1994, Vol. 368, **317**

30.) S. A. Bagshaw, E. Prouzet, T. J. Pinnavaia, Templating of Mesoporous Molecular Sieves by Nonionic Polyethylene Oxide Surfactants. *Science*, 1995, Vol. 269, **1242**

31.) P. T. Tanev, T. J. Pinnavaia, A Neutral Templating Route to Mesoporous Molecular Sieves. *Science*, 1995, Vol. 267, 865

32.) A. Firouzi, F. Atef, A. G. Oertli, G. D. Stucky, B. F. Chmelka, Alkaline Lyotropic Silicate-Surfactant Liquid Crystals. *J. Am. Chem. Soc.,* 1997, Vol. 119, **3596**

33.) G. D. Stucky, Q. Huo, A. Firouzi, B. F. Chmelka, S. Schacht, I. G. Voight-Martin, F. Schuth, Progress in Zeolite and Other Microporous Materials, *Stud. Surf. Sci. Catal*., 1996, Vol. 105, **3**

34.) C.F. Cheng, Z. Luan, J. Klinowski, The Role of Surfactant Micelles in the Synthesis of the Mesoporous Molecular Sieve MCM-41**,** *Langmuir*, 1995, Vol. 11(7), **2815**

35.) J. N. Israelachvili, D. J. Mitchell, B. W. Ninham, Theory of Self-Assembly of Hydrocarbon Amphiphiles into Micelles and Bilayers, *J. Chem. Soc. Faraday Trans. 2.*, 1976, Vol. 72, **1525**

36.) J. N. Israelachvili, *Intermolecular and Surface Forces*, 1st Edition, London: London Academic Press, 1991

37.) P. Behrens, A. Glaue, C. Haggenmuller, G. Schechner, Structure-Directed Materials Syntheses: Synthesis Field Diagrams for the Preparation of Mesostructured Silicas, *Solid State Ionics*, 1997, Vol. 101-103**, 255**

38.) G. D. Stucky, A. Monnier, F. Schuth, Q. Huo, D. Margolese, D. Kumar, M. Krishnamurty, P. Petroff, A. Firouzi, A. Janicke, B. F. Chmelka, Molecular and Atomic Arrays in Nano- and Mesoporous Materials Synthesis, *Mol. Cryst. Liq. Cryst*., 1994, Vol. 240, **187**

39.) A. Firouzi, D. Kumar, L. Bull, T. Besier, P. Sieger, Q. Huo, S. Walker, J. Zasadzinski, C. Glinka, J. Nicol, D. Margolese, G. D. Stucky, B. Chmelka, Cooperative Organization of Inorganic-Surfactant and Biomimetic Assemblies. *Science*, 1995, Vol. 267, **1138**

40.) J. C. Vartuli, K. D. Schmidt, C. T. Kresge, W. J. Roth, M. E. Leonowicz, S. B. McCullen, S. D. Hellring, J. S. Beck, J. L. Schlenker, D. H. Olson, E. W. Sheppard, Effect of Surfactant/Silica Molar Ratios on the Formation of Mesoporous Molecular Sieves: Inorganic Mimicry of Surfactant Liquid-Crystal Phases and Mechanistic Implications, *Chem. Mater*., 1994, Vol. 6, **2317**

41.) B. D. Cullity, *Elements of X-ray Diffraction*, 2nd Edition, Addison Wesley Longman Publishing Company, 1978

42.) V. B. Fenelonov, V. N. Romannikov, A. Y. Derevyankin, Mesopore Size and Surface Area Calculations for Hexagonal Mesophases (Types MCM-41, FSM-16, etc.) Using Low-Angle XRD and Adsorption Data, *Microporous and Mesoporous Mater*., 1999, Vol. 28, **57**

43.) K. J. Elder, J. W. White, Further Improvements in the Long-Range Order of MCM-41 Materials, *Chem. Mater*., 1997, Vol. 9, **1226**

44.) A. Corma, From Microporous to Mesoporous Molecular Sieve Materials and Their Use in Catalysis, *Chem. Rev*., 1997, **97**, 2373

45.) A. Doyle, B. K. Hodnett, Preparation Dependent Parameters of Mesoporous Silicates, *Book of Abstracts*, *Europacat V*, September 2001, University of Limerick, Ireland, Symp. 1, **43**

46.) S. Schacht, M. Janicke and F. Schüth, Modeling X-ray Patterns and TEM Images of MCM-41, *Microporous and Mesoporous Mater.*, 1998, Vol. 22, **485**

47.) S. Lowell, *Introduction to Powder Surface Area*, New York, Wiley Interscience, 1979

48.) S. Brunauer, L. S. Deming, W. S. Deming, E. Teller, On a Theory of the van der Waals Adsorption of Gases, *J. Am. Chem. Soc.*, 1940, Vol. 62, **1723**

49.) A. Baiker, *International Chemical Engineering*, 1985, **25**, 16

50.) I. Langmuir**,** The Constitution and Fundamental Properties of Solids and Liquids. Part I: Solids. *J. Am. Chem. Soc.*, 1916, Vol. 38, **2221**

51.) T. Allen, *Particle Size Measurement,* 3rd Edition, London, Chapman and Hall, 1981

52.) S. Brunauer, P. H. Emmet, E. Teller, Adsorption of Gases in Multimolecular Layers, *J. Am. Chem. Soc.*, 1938,Vol. 60, **309**

53.) K. K. Aligizaki, *Pore Structure of Cement-Based Materials Testing, Interpretation and Requirements,* Oxon Taylor and Francis, 2006

54.) S. J. Gregg, K. S. W. Sing, *Adsorption, Surface Area, and Porosity,* 2nd Edition, London, Academic Press, 1982

55.) A. Zsigmondy, *Z. Anorganisch Chemie*, 1911, **71**, 356

56.) E. P. Barrett, L. G. Joyner, P. P. Halenda**,** The Determination of Pore Volume and Area Distributions in Porous Substances. I. Computations from Nitrogen Isotherms, *J. Am. Chem. Soc.*, 1951, Vol. 73, **373**

57.) M. Kruk, M. Jaroniec, A. Sayari, Application of Large Pore MCM-41 Molecular Sieves To Improve Pore Size Analysis Using Nitrogen Adsorption Measurements, *Langmuir,* 1997, Vol. 13, **6267**

58.) P. J. Branton, P. G. Hall, K. S. W. Sing, Physisorption of Nitrogen and Oxygen by MCM-41, a Model Mesoporous Adsorbent, *J. Chem. Soc. Chem. Comm.*, 1993, **1257**

59.) P. J. Branton, P. G. Hall, K. S. W. Sing, H. Reichert, F. Schuth, K. K. Unger, Physisorption of Argon, Nitrogen and Oxygen by MCM-41, a Model Mesoporous Adsorbent, *J. Chem. Soc. Faraday Trans*., 1994, Vol. 19, **2956**

60.) O. Franke, G. Schulz-Ekloff, J. Rathousky, J. Starck, A. Zukal, Unusual Type of Adsorption Isotherm Describing Capillary Condensation Without Hysteresis, *J. Chem. Soc. Chem. Comm*., 1993, **724**

61.) R. Schmidt, M. Stocker, E. Hansen, D. Akporiaye, O. H. Ellestad, X-ray Absorption Spectroscopic Study on the Structure and Crystallization of Ga-Containing MFI-Type Zeolites, *Microporous Mater*., 1995, Vol. 3, **443**

62.) C.-Y. Chen, H.-X. Li, M. E. Davis, Studies on Mesoporous Materials : I. Synthesis and Characterization of MCM-41, *Microporous Mater*., 1993, **2**, 17

63.) P. I. Ravikovitch, D. Wei, W. T. Chueh, G. L. Haller, A. V. Neimark, Evaluation of Pore Structure Parameters of MCM-41 Catalyst Supports and Catalysts by Means of Nitrogen and Argon Adsorption, *J. Phys. Chem. B*, 1997, Vol. 101, **3671**

64.) P. L. Llewellyn, Y. Grillet, F. Schuth, H. Reichert, K. K. Unger, Effect of Pore Size on Adsorbate Condensation and Hysteresis Within a Potential Model Adsorbent: M41S, *Microporous Mater*., 1994, Vol. 3, **345**

65.) J. Rathousky, A. Zukal, O. Franke, G. Schulz-Ekloff, Adsorption on MCM-41 Mesoporous Molecular Sieves. Part 2: Cyclopentane Isotherms and Their Temperature Dependence, *J. Chem. Soc. Faraday Trans*., 1995, Vol. 91, **937**

66.) P. I. Ravikovitch, S. C. O'Domhnaill, A. V. Neimark, F. Schuth, K. K. Unger, Capillary Hysteresis in Nanopores: Theoretical and Experimental Studies of Nitrogen Adsorption on MCM-41, *Langmuir*, 1995, Vol. 11, **4765**

67.) J. Rathousky, A. Zukal, O. Franke, G. Schulz-Ekloff, Adsorption on MCM-41 Mesoporous Molecular Sieves. Part 1: Nitrogen Isotherms and Parameters of the Porous Structure, *J. Chem. Soc. Faraday Trans*., 1994, Vol. 90, **2821**

68.) M. Kruk, M. Jaroniec, A. Sayari, Adsorption Study of Surface and Structural Properties of MCM-41 Materials of Different Pore Sizes, *J. Phys. Chem. B,* 1997, Vol. 101, **583**

69.) C.J.Brinker, Porous inorganic materials, *Current Opinion in Solid State and Materials Science*, 1996, Vol. 1, Issue 6, **798-805**

70.) C. Y. Chen, S.-Q. Xiao, M. E. Davis, Studies on Ordered Mesoporous Materials III. Comparison of MCM-41 to Mesoporous Materials Derived from Kanemite, *Microporous Mater*., 1995, Vol. 4, **1**

71.) V. Alfredsson, M. Keung, A. Monnier, G.D. Stucky, K.K. Unger, F. Schuth, High-Resolution Transmission Electron Microscopy of Mesoporous MCM-41 Type Materials, *J. Chem. Soc. Chem. Comm*., 1994, **921**

72.) A. Chenite, Y. LePage, A. Sayari, Direct TEM Imaging of Tubules in Calcined MCM-41 Type Mesoporous Materials, *Chem. Mater*., 1995, Vol. **7**, **1015**

73.) J. Feng, Q. Huo, P. M. Petroff, G. D. Stucky, Morphology Definition by Disclinations and Dislocations in a Mesostructured Silicate Crystal, *Appl. Phys. Lett*., 1997, Vol. 71, **620**

74.) U. Ciesla, F. Schuth, Ordered Mesoporous Materials, *Microporous and Mesoporous Mater*., 1999, Vol. 27, **131**

75.) Z. Jin, X. Wang, X. Cui, Synthesis and morphological investigation of ordered SBA-15-type mesoporous silica with an amphiphilic triblock copolymer template under various conditions, *Colloids and Surfaces A: Physicochemical and Engineering Aspects*, 2008,Vol. 316, Issues 1-3, **27-36**

76.) M.S. Cho, H.J. Choi, K.Y. Kim, W.S. Ahn, Synthesis and Characterization of Polyaniline/Mesoporous SBA-15 Nanocomposite, *Macromolecular Rapid Communications*, 2002, Vol. 23 Issue 12, **713-716**

77.) J. Goldstein, D.E. Newbury, D.C. Joy, P. Echlin, C.E. Lyman, E.Lifshin, L.Sawyer, *Scanning electron microscopy and x-ray microanalysis*, 3rd edition, Springer Science, U.S.A., 2003

78.) M.K. Naskar, M. Eswaramoorthy, Significant improvement in the pore properties of SBA-15 brought about by carboxylic acids and hydrothermal treatment, *J. Chem. Sci.*, 2008, Vol. 120 (1), **181–186.**

79.) R.F. Egerton, *Physical principles of electron microscopy: an introduction to TEM, SEM, and AEM*, Springer Science and Business Media, U.S.A. 2005.

80**)** R. Chang, *Chemistry*, 4th edition, McGraw-Hill, New Jersey U.S.A. 1991

81) P. Delhaès, *Graphite and Precursors*, Gordon and Breach Science Publishers, New York, 2001

82) H. Zaïdi, H. Néry, and D. Paulmier, Stability of lubricating properties of graphite by orientation of the crystallites in the presence of water vapour, *Applied Surface Science*, 1993, Vol. 70-71(1), **180-185**

83) R. Harwood, *Physical Geology 101[Online]*, Black Hawk College Employee Learning Centre Ilannois, Available at: http://facweb.bhc.edu/academics/science/harwoodr/geol101/study/Images/graphite.jpg, [Accessed Apr 2010].

84) H.W. Kroto, J.R. Heath, S.C. O'Brien, R.F. Curl, and R.E. Smalley, C_{60}: Buckminsterfullerene, *Nature*, 1985, Vol. 318, **162-163.**

85) P. Kent, *C60*, Oak Ridge National laboratory Tennessee, available at: http://www.ornl.gov/~pk7/pictures/c60.html, [Accessed: December 2011]

86) H. Kietzmann, R. Rochow, G. Ganteför, W. Eberhardt, K. Vietze, G. Seifert and P. W. Fowler, Electronic Structure of Small Fullerenes: Evidence for the High Stability of C_{32}, *Phys. Rev. Lett*., 1998, Vol. 81, **5378-5381.**

87) H. Handschuh, P. S. Bechthold, B. Kessler, G. Ganteför, and W. Eberhardt, Stable Configurations of Carbon Clusters: Chains, Rings, and Fullerenes, *Phys. Rev. Lett.* 1995, Vol. 74, **1095-1098**

88) J.R. Heath, Synthesis of C_{60} From Small Carbon Clusters: A Model Based on Experiment and Theory. In "Fullerenes: Synthesis, Properties and Chemistry of Large Carbon Clusters", *ACS Symp. (ed. G. S. Hammond and V.J. Kuck*), 1992, Ser. 481, **1-23.**

89) P.W. Fowler and D.E. Manolopoulos, *An Atlas of Fullerenes*, Clarendon Press, Oxford, 1995.

90) M.S. Dresselhaus, G. Dresselhaus and P.C. Ecklund, *Science of Fullerenes and Carbon Nanotubes*: *Their Properties and Applications,* Academic Press, U.S.A. 1996

91) P. R. C. Kent, M. D. Towler, R. J. Needs, and G. Rajagopal, Carbon clusters near the crossover to fullerene stability, *Phys. Rev. B.*, 2000, Vol 62 (23), **15394-15397**

92) P. Hollister, C. Román Vas, T. Harper, Fullerenes, *Cientifica, Technology White Paper* No. 7, 2003.

93.) L.S. Pan, D.R. Kania (Eds.), *Diamond: Electronic Properties and Applications*, Kluwer Academic Publishers, Boston,1995.

94.) W. Yarbrough, R. Messier, Current Issues and Problems in the Chemical Vapor Deposition of Diamond: *Science*, 1990, Vol. 247, **688.**

95.) J.C. Angus, C.C. Hayman, Low-Pressure, Metastable Growth of Diamond and "Diamondlike" Phases, *Science*, 1988, Vol. 241, **913**.

96.) J. Wilks, E. Wilks (Eds.), *Properties and Application of Diamond*, Butterworth Heinemann Ltd. Oxford (UK), 1991.

97.) R.F. Davis (Ed.), *Diamond Films and Coatings*, Noyes Publications, New Jersey, 1992.

98.) J.E. Field, *The Properties of Diamond*, Academic Press, Oxford, 1979.

99.) S.T. Lee, Z.D. Lin, X. Jiang, CVD diamond films: nucleation and growth *Mater. Sci. Eng. R:Reports*, 1999, Vol. 25 (4), **123-154**.

100.) C.X. Wang, G.W. Yang, T.C. Zhang, H.W. Liu, Y.H. Han, J.F. Lou, C.X. Gao, G.T. Zou, High-quality heterojunction between *p*-type diamond single-crystal film and *n*-type cubic boron nitride bulk single crystal *Appl. Phys. Lett*. 2003, Vol. 83 **4854**.

101.) C.X. Wang, G.W. Yang, H.W. Liu, Y.H. Han, J.F. Lou, C.X. Gao, G.T. Zou, Experimental analysis and theoretical model for anomalously high ideality factors in ZnO/diamond *p-n* junction diode, *Appl. Phys. Lett*. 2004, Vol. 84, **2427**.

102.) C.X. Wang, G.W. Yang, C.X. Gao, H.W. Liu, Y.H. Han, J.F. Luo, G.T. Zou, Highly oriented growth of n-type ZnO films on p-type single crystalline diamond films and fabrication of high-quality transparent ZnO/diamond heterojunction, *Carbon*, 2004, Vol. 42, **317-321.**

103.) C.X. Wang, G.W. Yang, T.C. Zhang, H.W. Liu, Y.H. Han, J.F. Luo, C.X. Gao, G.T. Zou, Preparation of low-threshold and high current rectifying heterojunction using B-doped diamond grown on Si-treated c-BN crystals, *Diamond Relat. Mater*. 2003, Vol. 12, **1422-1425.**

104.) C.X. Wang, G.W. Yang, T.C. Zhang, H.W. Liu, Y.H. Han, J.F. Luo, C.X. Gao, G.T. Zou, Fabrication of transparent p-n hetero-junction diodes by p-diamond film and n-ZnO film, *Diamond Relat. Mater.* 2003, Vol. 12, **1548-1552.**

105.) C.X.Wang, C.X. Gao, T.C. Zhang, H.W. Liu, X. Li, Y.H. Han, J.F. Luo, C.X. Shen, Preparation of p-n Junction Diode by B-Doped Diamond Film Grown on Si-Doped c-BN, *Chin. Phys. Lett*., 2002, Vol. 19, **1513.**

106.) C.X. Wang, C.X. Gao, H.W. Liu, Y.H. Han, J.F. Luo, C.X. Shen, Preparation and Transparent Property of the n-ZnO/p-Diamond Heterostructure, *Chin. Phys. Lett.* 2003, Vol. 20, **127.**

107.) C.X. Wang, T.C. Zhang, H.W. Liu, C.X. Gao, G.T. Zou, Diamond films grown on seeded substrates by hot-filament chemical vapour deposition with H2 as the only feeding gas, *J. Phys.: Condens. Matter*., 2002, Vol. 14, **10969**.

108) S. Sque, *Structure of Diamond*[Online], University of Exeter: AIMpro Group. Available at: http://newton.ex.ac.uk/research/qsystems/people/sque/diamond/structure/, 2006, [Accessed: August 2009]

109.) C. X. Wang, G. W. Yang, Thermodynamics of metastable phase nucleation at the nanoscale, Materials Sciences and Engineering, 2005, R49, 157-202.

110.) A. Yarnell, The Many Facets of Man-made Diamonds, *Chemical and Engineering News*, 2004, Vol. 82(5), **26-31.**

111.) F.P. Bundy, H.T. Hall, H.M. Strong, R.H. Wentorf, Man-made Diamonds, *Nature*, 1955, Vol. 176, **51-55**.

112.) W. Kern, V. S. Ban, *Chemical Vapour Deposition of Inorganic Thin Films in Thin Film Process*, ed. By J. L. Vossen and W. Kern. Academic Press New York, 1978 **258**

113.) M. N. R. Ashfold, P. W. May, C. A. Rego, Thin Film Diamond by Chemical Vapour Deposition Methods, *Chemical Society Reviews*, 1994, Vol. 23, **21-30.**

114.) S. Matsumoto, Y. Sato, M. Tsutsumi, N. Setaka, Growth of diamond particles from methane-hydrogen gas, *Journal of Materials Science*, 1982, Vol. 17(11), **3106.**

115.) S. T. Lee, Z. Lin, X. Jiang, CVD diamond films: nucleation and growth *Materials Science and Engineering: R: Reports*, 1999, Vol. 25(4), **123-154**

116.) H.O. Pierson, *Handbook of Chemical vapour deposition*: *Principles, Technology and Applications.* 2nd edition. Noyes Publications, William Andrew Publishing U.S.A., 1999.

117.) K. Kearney, ECR Finds Applications in CVD, *Semiconductor International*, 1989.

118.) Y.Z. Hu, M. Li, J. Sunko, J. Andrews, E. Irene, Characterization of Microwave ECR Plasma for Low Temperature Chemical Vapour Deposition, *Proc. 11th Int. Conf. on CVD*. 1990, **166-172.**

119.) P.K. Bachman, G. Gartner, H. Lydtin, Plasma-Assisted Chemical Vapour Deposition, *MRS Bulletin,* 1988, **52-59.**

120.) Y. Hirose, New Diamond Forum, *1st Intern. Conf. on the New Diamond Sci Technol.*, Japan, 1988, **38.**

121.) K.V. Ravi, C.A. Koch, Nucleation enhancement of diamond synthesized by combustion flame techniques, *Appl. Phys. Lett.*, 1990, Vol 57(4), **348-350**

122.) B.V. Spitzyn, L.L. Bouilov, B.V. Derjaguin, Vapour growth of diamond on diamond and other surfaces, *J. Crystal Growth*, 1981, Vol 52, **219-226.**

123.) E. Kondoh, K. Tanaka, T. Ohta, Homeoepitaxial growth of diamond by an advanced hot-filament chemical vapour deposition method, *J. Appl. Phys.*, 1993, Vol. 74(3), **2030-2035.**

124.) M.P. D'Evelyn, C.J. Chu, R.H. Hange, J.L. Margrave, Mechanism of diamond growth by chemical vapour deposition: carbon-13 studies, *J. Appl. Phys.*, 1992, Vol. 71(3), **1528-1530.**

125.) C.J. Chu, M.P. D'Evelyn, R.H. Hange, J.L. Margrave, Mechanism of diamond growth by chemical vapour deposition on diamond (100), (111), and (110) surfaces: carbon-13 studies, *J. Appl. Phys.*, 1991, Vol. 70(3), **1695-1705.**

126.) J.E. Field, *The Properties of Diamond*, Academic Pres, London, 1979

127.) J. Kim, M. Kim, S. Park, J. Lee, The morphology changes in diamond synthesized hot-filament chemical vapour deposition, *J. Appl. Phys.*, 1990, Vol. 67(7), **3354-3357.**

128) B.V. Derjaguina, D.V. Fedoseeva, V.M. Lukyanovicha, B.V. Spitzina, V.A. Ryabova and A.V. Lavrentyeva, Filamentary diamond crystals, *Journal of Crystal Growth*, 1968, Vol 2(6), **380-384**

129) R.S. Wagner, and W.C. Ellis, Vapor-liquid-solid mechanism of single crystal growth, *Appl. Phys. Lett.* 1964, Vol. 4(5), **89-91**.

130) A. S. Barnard, Structural Properties of Diamond Nanowires: Theoretical Predictions and Experimental Progres, *Rev. Adv. Mater. Sci*., 2004, Vol. 6, **94-119**

131) E. S. Baika, Y. J. Baika, S. W. Leeb and D. Jeon, Fabrication of diamond nano-whiskers, *Thin Solid Films*, 2000, Vol. 377-378, **295-298**

132) H. Masuda, T. Yanagishita, K. Yasui, K. Nishio, I. Yagi, T. N. Rao, A. Fujishima, Synthesis of Well-Aligned Diamond Nanocylinders, *Advanced Materials*, 2001, Vol. 13(4**),** **247-249**

133) M. L. Terranova,* S. Orlanducci, A. Fiori, E. M. Rossi , and A. S. Barnard Controlled evolution of carbon nanotubes coated by nanodiamond: the realization of a new class of hybrid nanomaterials, *Chem. Mater.*, 2005, Vol.17 (12), **3214–3220**

134) LT Sun, JL Gong, DZ Zhu, ZY Zhu, SX He, Diamond nanorods from carbon nanotubes. *Advanced Materials*, 2004, Vol. 16(20), **1849-1853**

135) I. Vlasov, O. I. Lebedev, V. G. Ralchenko, E. Goovaerts, G. Bertoni, G. Van Tendeloo, and V. I. Konov, Hybrid Diamond-Graphite Nanowires Produced by Microwave Plasma Chemical Vapor Deposition, *Adv. Mater.* 2007, Vol. 19(22), **4058-4062**

136) A.S Barnard, S.P. Russo, Ab-initio modelling of diamond nanowire structures, *Nano Lett.* 2003, Vol. 3(10), **1323-1328**

137) O. Shenderova, D. Brenner, and R. S. Ruoff, Would Diamond Nanorods Be Stronger than Fullerene Nanotubes? *Nano Letters*, 2003, Vol. 3(6), **805–809**

138) N. Dubrovinskaia, L. Dubrovinsky, W. Crichton, F. Langenhorst, and A. Richter, Aggregated diamond nanorods, the densest and least compressible form of carbon. *Appl. Phys. Lett.* 2005, Vol. 87, **083106**

139.) M.S. Kang, W.S. Lee, and Y.J. Baik, Morphology variation of diamond with increasing pressure up to 400 torr during deposition using hot filament CVD, *Thin Solid Films*, 2001, Vol. 398-399, **175-179**

140.) I. U. Hassan, C. A. Rego, N. Ali, W. Ahmed, and I. P. O'Hare, An Investigation of the Structural Properties of Diamond Films Deposited by Pulsed Bias Enhanced Hot Filament CVD, *Thin Solid Films*, 1999, Vol. 355-356, **134-138**

141.) H. C. Shih, C. P. Sung, W. T. Hsu, S. L. Sung, C. T. Hwang, H. F. Hsieh, and W. L. Fan, The dilution effect of noble gases on the structure and composition of chemically vapour-deposited diamond films, *Diamond and Related Materials*, 1993, Vol. 2(3-4), **531-536**